The Astrophysical Journal, 975:213 (21pp), 2024 November 10 https://doi.org/10.3847/1538-4357/ad7d83

Impact of Systematic Modeling Uncertainties on Kilonova Property Estimation

D. Brethauer[1], D. Kasen[2], R. Margutti[1,2], and R. Chornock[1]
[1] Department of Astronomy, University of California, Berkeley, CA 94720-3411, USA; daniel_brethauer@berkeley.edu
[2] Department of Physics, University of California, 366 Physics North MC 7300, Berkeley, CA 94720, USA
Received 2024 August 12; revised 2024 September 16; accepted 2024 September 18; published 2024 November 5

Abstract

The precise atomic structure and therefore the wavelength-dependent opacities of lanthanides are highly uncertain. This uncertainty introduces systematic errors in modeling transients like kilonovae and estimating key properties such as mass, characteristic velocity, and heavy metal content. Here, we quantify how atomic data from across the literature as well as choices of thermalization efficiency of *r*-process radioactive decay heating impact the light curve and spectra of kilonovae. Specifically, we analyze the spectra of a grid of models produced by the radiative transfer code `Sedona` that span the expected range of kilonova properties to identify regions with the highest systematic uncertainty. Our findings indicate that differences in atomic data have a substantial impact on estimates of lanthanide mass fraction, spanning approximately 1 order of magnitude for lanthanide-rich ejecta, and demonstrate the difficulty in precisely measuring the lanthanide fraction in lanthanide-poor ejecta. Mass estimates vary typically by 25%–40% for differing atomic data. Similarly, the choice of thermalization efficiency can affect mass estimates by 20%–50%. Observational properties such as color and decay rate are highly model dependent. Velocity estimation, when fitting solely based on the light curve, can have a typical error of ∼100%. Atomic data of light *r*-process elements can strongly affect blue emission. Even for well-observed events like GW170817, the total lanthanide production estimated using different atomic data sets can vary by a factor of ∼6.

Unified Astronomy Thesaurus concepts: High energy astrophysics (739); Gravitational wave sources (677); Transient sources (1851); Time domain astronomy (2109)

1. Introduction

Compact-object mergers involving a neutron star (NS) have long been at the forefront of high-energy phenomena, from short gamma-ray bursts (e.g., D. Eichler et al. 1989; R. Narayan et al. 1992) to sites of rapid neutron capture (*r*-process) nucleosynthesis (J. M. Lattimer & D. N. Schramm 1974, 1976; E. Symbalisty & D. N. Schramm 1982; D. Eichler et al. 1989; C. Freiburghaus et al. 1999; S. Rosswog et al. 1999). The discovery of gravitational wave source GW170817 and its electromagnetic counterparts AT2017gfo, GRB170817A, and the resulting afterglow (B. P. Abbott et al. 2017; K. D. Alexander et al. 2017; I. Andreoni et al. 2017; I. Arcavi et al. 2017; R. Chornock et al. 2017; D. A. Coulter et al. 2017; P. S. Cowperthwaite et al. 2017; M. C. Díaz et al. 2017; M. R. Drout et al. 2017; P. A. Evans et al. 2017; A. Goldstein et al. 2017; G. Hallinan et al. 2017; L. Hu et al. 2017; M. M. Kasliwal et al. 2017; V. M. Lipunov et al. 2017; R. Margutti et al. 2017; E. Pian et al. 2017; V. Savchenko et al. 2017; B. J. Shappee et al. 2017; S. J. Smartt et al. 2017; M. Soares-Santos et al. 2017; N. R. Tanvir et al. 2017; E. Troja et al. 2017; Y. Utsumi et al. 2017; S. Valenti et al. 2017; A. S. Pozanenko et al. 2018; S. Sugita et al. 2018) confirmed the connection between compact objects and some short gamma-ray bursts (GRBs), ushering in a new era transient multimessenger astronomy (see R. Margutti & R. Chornock 2021 and E. Nakar 2020 for detailed reviews). The multi-wavelength electromagnetic radiation from AT2017gfo was the kilonova (KN), which is mainly powered by the radioactive decay of *r*-process material, and lasted between days and weeks depending on the wavelength at which it was observed (V. A. Villar et al. 2017 and references therein). AT2017gfo provided an unprecedented amount of data, and represents one realization of KN emission in the broader phase space of potential KN emission. Theory predicts and observations have shown a wide diversity of KN emission as a direct result of the three main properties of the ejecta launched during and after the merger event: the mass, characteristic velocity, and heavy-metal content (typically denoted as the mass fraction of lanthanides, $X_{\rm lan}$, a product of *r*-process nucleosynthesis).

Encoded within the KN spectra is information about the compact objects that created them and the fate of the remnant (e.g., D. Kasen et al. 2017; D. Radice et al. 2020; D. Radice & S. Bernuzzi 2023) as well as the evolution of the heavy-metal content of the Universe (e.g., Y. Z. Qian & G. J. Wasserburg 2007; K. Hotokezaka et al. 2015; A. Wallner et al. 2015; A. P. Ji et al. 2016; S. Rosswog et al. 2018). In order to make meaningful progress on extracting this information, both high accuracy and high precision measurements are required. However, to construct simulations and models of KNe, astronomers are required to make numerous choices for prescriptions concerning the heating rate from the decay of *r*-process material (J. Lippuner & L. F. Roberts 2015; Y. L. Zhu et al. 2021; N. Sarin & S. Rosswog 2024), *r*-process decay products (Y. L. Zhu et al. 2021), the velocity profile of the ejecta (e.g., C. L. Fryer et al. 2024), how efficiently the radioactive decay products of *r*-process material deposit their energy into the ejecta (J. Barnes et al. 2016; S. Rosswog et al. 2017; M. Bulla 2023), the multidimensional structure of the ejecta (e.g., K. Kawaguchi et al. 2018; R. T. Wollaeger et al. 2021; L. J. Shingles et al. 2023; M. Bulla 2023), or the distribution of lanthanide-rich material within the ejecta as a function of radius (D. Kasen et al. 2017).

Another such assumption regards how the products of *r*-process nucleosynthesis interact with the radiation of the KN. The presence of a high lanthanide fraction manifests as an infrared-bright transient, due to the extremely high opacity ($\gtrsim 10^2$ cm^2 g^{-1}) in the optical and UV from the valence *f*-shell electron of lanthanide elements (i.e., D. Kasen et al. 2013; C. J. Fontes et al. 2020; M. Tanaka et al. 2020). Despite the importance of the lanthanides in creating the characteristic *r*-process infrared excess, the precise atomic structure of these elements is highly uncertain, resulting in highly uncertain opacities (D. Kasen et al. 2013). This uncertainty introduces an additional systematic error source into modeling KNe that we quantify here by using three sets of atomic structure data produced from various codes (further explained in Section 3.1).

Additionally, as radioactive isotopes generated from *r*-process decay, they release energy in the form of neutrinos, alpha particles, beta particles, gamma-rays, and fission fragments. Each species deposits a varying fraction of its energy into the ejecta. To analytically describe this variable energy deposition, we use two different prescriptions: a global mass-averaged efficiency where all zones have the same thermalization efficiency (i.e., J. Barnes et al. 2016), and a local density-based efficiency (i.e., J. Barnes et al. 2016; M. Bulla 2023) where the thermalization efficiency is based on the local conditions in each zone (further explained in Section 3.2). Each approach leads to a different energy budget for the KN to emit, which alters the resulting spectra and similarly creates a systematic error source that we quantify here.

In Section 2, we discuss the setup of our radiative transfer code simulations and the chosen range of ejecta parameters. In Section 3, we discuss the different atomic data we vary as well as the thermalization prescriptions. In Section 4, we present the variance in the resulting light curves and spectra from the different atomic data sets and thermalization prescriptions. In Section 5, we quantify the error in parameter estimation based on atomic data set and thermalization prescription. Finally, we summarize our findings in Section 6.

2. Sedona and Initial Conditions Setup

We use the Monte Carlo radiative transfer code `Sedona` (D. Kasen et al. 2006; N. Roth & D. Kasen 2015) to generate synthetic spectra, from which we derive light curves and bolometric luminosities. We explore a grid of models using $M \in [0.001, 0.01, 0.1]\ M_\odot$, $v_k \in [0.1, 0.3]\ c$, and $\log_{10}(X_{\rm lan}) \in [-9, -4, -2]$ (where M is the total ejecta mass, v_k is the characteristic velocity of the ejecta defined as $v_k = \sqrt{\frac{2E_k}{M}}$ and E_k is the total kinetic energy, and c is the speed of light). The range of this grid is motivated by observational KN parameter estimates of AT2017gfo (e.g., V. A. Villar et al. 2017; M. W. Coughlin et al. 2018; M. Ristić et al. 2023), GRMHD simulations of compact object merger events (e.g., D. Radice et al. 2020), and nucleosynthetic yields of *r*-process ejecta (e.g., J. Lippuner & L. F. Roberts 2015). We generate synthetic spectra for each combination of atomic data and thermalization efficiency prescription to explore the impact on a wide extent of expected theoretical KN emission.

We run each simulation as a spherically symmetric model with 80 zones that are expanding homologously defined by a temperature, density, velocity, composition, and size. We initialize the model at time $t_0 = 0.25$ day after the merger, early enough that radiative diffusion will not yet have caused substantial energy loss, and `Sedona` homologously expands the initial conditions while dynamically evolving the properties of each zone (or contracts in the case of simulating earlier times). Homologous expansion sets in on a dynamical timescale that is $\approx$1 s, which is well before we initialize each simulation. The density of each zone is defined by a broken power law

$$\rho(v) = \begin{cases} \eta_\rho \dfrac{M}{v_t^3 t^3} \left(\dfrac{v}{v_t}\right)^{-\delta} & v \leqslant v_t \\ \eta_\rho \dfrac{M}{v_t^3 t^3} \left(\dfrac{v}{v_t}\right)^{-n} & v > v_t, \end{cases} \quad (1)$$

where δ and n are the power-law index of the inner and outer ejecta, respectively, v_t is the transition velocity between the two power-law indices, M is the total mass, t is time, and η_ρ is the normalization constant. Following D. Kasen et al. (2017), we adopt $\delta = 1$ and $n = 10$ as the broken power-law density profile arises from disk models (e.g., the velocity distributions studied in C. L. Fryer et al. 2024). The transitional velocity, v_t, is defined as

$$v_t = \eta_v v_k = \eta_v \sqrt{\frac{2E_k}{M}}, \quad (2)$$

where η_v is the normalization constant to ensure the ejecta has total kinetic energy E_k. The maximum velocity of each model is $3v_t$ for $0.1c$ models and $2v_t$ for $0.3c$ models, as after the transition velocity the steep $n = 10$ power-law decline in density rapidly makes the outermost ejecta mass negligible.

The composition of each model is based on solar abundance patterns (or meteoric in cases where solar abundances are not available) presented in M. Asplund et al. (2009), and *r*-process residuals from J. Simmerer et al. (2004) for elements with atomic number $Z = 31$–70. This differs from the models presented in D. Kasen et al. (2017), which use an even distribution of nonlanthanide material as opposed to solar abundance patterns. The composition is then normalized by mass fraction such that all elements of $Z = 58$–70 have a total mass fraction of $X_{\rm lan}$ and all other elements have a total mass fraction of $1 - X_{\rm lan}$. We do not consider any elements of $Z \geqslant 71$.

The level populations of each element are determined by Local Thermodynamic Equilibrium (LTE). We expect non-LTE (NLTE) effects to begin affecting the spectra on a timescale by which the majority of the mass in the ejecta is optically thin as determined by

$$t_{\rm NLTE} \approx 7.2 \left(\frac{M_{ej}}{0.03 M_\odot}\right)^{0.5} \left(\frac{\kappa}{1\ {\rm cm^2\ g^{-1}}}\right)^{0.5} \left(\frac{v_k}{0.1c}\right)^{-1} {\rm days}, \quad (3)$$

where M_{ej} is the total mass ejected, κ is the opacity of the material, and v_k is the characteristic velocity. Beyond this timescale, the spectra will become less accurate, though, for the purposes of comparing atomic data, can still be illuminating.

Each spectrum is calculated every 0.1 day starting from $t = 0.1$ day to 35 day with 1524 logarithmically spaced frequency points between 10^{13} and 2×10^{16} Hz. Following D. Kasen et al. (2017), we limit hydrodynamical time steps to 10% of the elapsed time, which is sufficient to resolve the expansion evolution of the ejecta. However, we do not include the physics of free neutron decay or shock breakout in order to isolate the effects of atomic structure and thermalization

efficiency, and so caution about the use of these models at times $t \lesssim 0.5$ day.

At each time step, Monte Carlo packets (effectively bundles of photons of a given wavelength that total up to a specified energy amount) are released in accordance to the *r*-process heating rate convolved with the thermalization efficiency and interact with a zone through scattering and absorption. Monte Carlo photons that reach the outer edge of the simulation (defined by the maximum velocity) escape the ejecta and are collected and binned in time and frequency to generate the spectral time series of the model, with all relevant Doppler shift and light travel-time effects taken into account for an observer infinitely far away.

3. Model Experimental Variables

We consider three sets of atomic data and two thermalization efficiency prescriptions for a total of six combinations. While bound–bound transitions from lanthanide species dominate the opacity, we still consider free–free and electron scattering opacities in each model as they become more important at longer wavelengths where lanthanides no longer dominate as strongly and are simple to include from their analytic formula. We do not consider bound-free absorption due to the dominance of bound–bound absorption from lanthanides (i.e., $\kappa_{bf,Nd} = 0$ at $\lesssim$15 eV while $\kappa_{bb,Nd} \approx 50\,\mathrm{cm^2\,g^{-1}}$ at line locations).

3.1. Atomic Data

We consider three atomic data sets that are commonly found across KN modeling literature and each take a unique approach to atomic modeling, which we label as follows:

1. Data set `HULLAC`—$Z = 31$–70 data presented in M. Tanaka et al. (2020);
2. Data set `ATOMIC`—$Z = 58$–70 data presented in C. J. Fontes et al. (2020);
3. Data set `Autostructure`—Code used in D. Kasen et al. (2017), Z= 13–28, 58–70.

Both atomic data sets Hebrew University Lawrence Livermore Atomic Code (`HULLAC`) and `Autostructure` employ the "Sobolev expansion opacity" for binning the large number of lines from lanthanides. The "Sobolev expansion opacity" utilizes the Sobolev approximation (V. V. Sobolev 1960) for bound–bound transitions, which is applicable when the thermal line width of a given line is negligible compared to that of the expansion velocity. This is true for KN ejecta, as the expansion velocity is typically of the order $10^3\,\mathrm{km\,s^{-1}}$ while the thermal velocities are of the order $1\,\mathrm{km\,s^{-1}}$ (D. Kasen et al. 2013). The lines are then binned within the broader frequency bins of the simulation. Atomic data set `ATOMIC` also bins the lines, but instead employs a "straight discretization" method that preserves the area under the opacity curve (C. J. Fontes et al. 2020).

We do not include atomic data sets constructed entirely from experimentally verified lines. While accurately producing the strongest features will generate more readily comparable spectra to observed KNe, the number of lines available for a given ion ($\sim$100 s) is insufficient, does not span the needed wavelength range, and is only available for a limited set of ions, preventing the generation of the overall opacity required to run our simulations. In order to generate an overall opacity that can be used in a simulation, calibrated lines could be integrated into the atomic data sets (as done by J. H. Gillanders et al. 2022), though this would dilute the calibrated lines with a forest of uncalibrated lines. Consequently, the lack of calibration in the atomic data sets used in this work means that the precise wavelength of any given feature will not be accurate, but the comparisons of qualitative structure of spectral features and the overall continuum and colors between atomic data sets and resulting uncertainties that we focus on in this work remain true. Including the limited number of calibrated lines may bring atomic data sets into closer alignment with each other and reduce modeling uncertainties, but the requirement of incorporating a forest of uncalibrated lines to generate the overall opacity will likely limit the reduction in modeling uncertainty. We leave the investigation of the impact of inclusion of calibrated data to future work.

3.1.1. Atomic Data Set `HULLAC`

M. Tanaka et al. (2018, 2020) generated theoretical atomic data using the `HULLAC` (A. Bar-Shalom et al. 2001) for elements $Z = 26$–88, up to triply ionized species, in a self-consistent and systematic way for a large number of elements. As stated in M. Tanaka et al. (2020), this implies that spectral features produced by this data set should not be used to identify elements in the spectra of real KNe, rather the ensemble of transitions represent what the general statistical properties of the elements are as they have not been calibrated to experimental wavelengths. For this work, we use elements $Z = 31$–70.

`HULLAC` assumes that the electron orbital functions are represented well by a single electron Dirac equation with a central-field potential that arises from spherically averaged electron–electron interactions plus that of the nuclear charge. Due to the aspherical nature of *p*, *d*, and *f* orbitals, this may alter the energy level of orbitals.

3.1.2. Atomic Data Set `ATOMIC`

All data for elements $Z = 58$–70 are derived from opacity tables provided at NIST-LANL (Y. Ralchenko et al. 2021), which provide the electron scattering, bound–bound, bound-free, and free–free opacities for up to triply ionized species over the same grid of $\frac{h\nu}{k_b T}$ where h is the Planck constant, ν is the frequency of the photon, k_b is the Boltzmann constant, and T is the temperature. Each opacity is binned to the frequency grid of our `Sedona` simulation, then bilinearly interpolated between (logarithmic) density and (linear) temperature points to calculate the opacity at any given temperature and density. The opacity contribution from each atomic species is then summed.

It is important to note that the opacities derived in the table assume a pure composition of each element, which will have a systematic offset from a mixed composition as the free electron density is set by the ionization structure of multiple elements in the mixed composition. The line-binned approach for bound–bound transitions presented in the opacity tables agree with the Sobolev approximation in the optically thin limit (C. J. Fontes et al. 2020), though tends to produce higher opacities in the optically thick regime due to the straight discretization method. However, C. J. Fontes et al. (2020) argue that this discrepancy in opacities in the optically thick regime may not be that important to accurately model KN emission because the

photons become trapped in the ejecta under those conditions. NIST-LANL only includes lanthanides and actinides, so we use the nonlanthanide elements binned as described in the section above.

When calculating the energy levels of low ionization states, ATOMIC also considers the difference between the calculated ionization potential and the experimental ionization potential provided by NIST. The energy levels of the calculated atoms are then shifted by the difference between the two, but are otherwise not calibrated to experimental wavelengths.

3.1.3. Atomic Data Set Autostructure

Data set Autostructure is the same atomic structure code that is utilized in D. Kasen et al. (2017) and was used to calculate KN spectra when it was the first to consider that lanthanides were an important source of opacity in NS mergers (D. Kasen et al. 2013). All lanthanide element data were produced with the Autostructure code (N. R. Badnell 2011) up to quadruple ionized species, while all other elements were sourced from the CMFGEN compilation (D. J. Hillier & T. Lanz 2001). The atomic data produced by Autostructure have been optimized to produce the correct ground and first two excited levels for the singly ionized element Nd while, for all other elements, only the ground state was optimized. Similarly to D. Kasen et al. (2017), we approximate elements heavier than $Z = 28$ as lighter elements (while maintaining their original total mass) since the behavior of the valence electron should remain similar across any individual column on the periodic table (e.g., Os and Fe as shown in D. Kasen et al. 2017).

3.2. Thermalization Efficiency Prescriptions

Each simulation receives an input of energy from the *r*-process heating rate that is convolved with a thermalization efficiency prescription. This thermalization prescription is either applied on a by-zone basis (local) or shared among all zones (global). We consider one *r*-process heating rate per unit mass for all models defined by

$$\dot{Q}_r = At^{\alpha} + B_1 e^{-t/\beta_1} + B_2 e^{-t/\beta_2} \tag{4}$$

where $A = 8.49 \times 10^9$ erg g^{-1} s^{-1}, α is -1.36, B_1 is 8.34×10^9 erg g^{-1} s^{-1}, β_1 is 3.63 days, B_2 is 8.86×10^8 erg g^{-1} s^{-1}, and β_2 is 10.8 days as defined by the heating rate per unit mass for material of electron fraction $Y_e = 0.13$, entropy per baryon of 32*k*, and expansion timescale 0.84 ms from J. Lippuner & L. F. Roberts (2015).

While N. Sarin & S. Rosswog (2024) have shown that variable heating rates can also introduce a considerable source of error in modeling KNe, we restrict our models to only one *r*-process heating rate to isolate the effects of thermalization efficiency on KN parameter estimation.

3.2.1. Global Thermalization Efficiency Prescription

For the global thermalization prescription, we use the analytical formula presented in J. Barnes et al. (2016) (their Equation (34)) to describe the thermalization efficiency of all radioactive decay products in the *r*-process material:

$$f_{\rm tot}(t) = 0.36\left[e^{-at} + \frac{\ln(1 + 2bt^d)}{2bt^d}\right], \tag{5}$$

where a, b, and d are determined by the total mass and characteristic velocity of the ejecta and $f_{\rm tot}(t)$ is the fraction of decay energy deposited in the ejecta divided by the total decay energy emitted. The values derived in J. Barnes et al. (2016) are an analytical fit to the total thermalization fraction determined from numerical simulations of KNe with different masses and velocities. Specifically, we use the values shown in Table 1 for random magnetic fields in our simulations. It is important to note that assumptions of magnetic field structure have the potential to have a significant impact on thermalization efficiency as particular magnetic field structures can allow for nonlocal energy deposition (e.g., J. Barnes et al. 2016). For any values and velocities between the presented values of the table, we bilinearly interpolate each parameter.

The formula includes neutrino losses and J. Barnes et al. (2016) find that the radioactive decay products carry approximately 20%, 45%, and 35% of the decay energy for beta particles, gamma-rays, and neutrinos, respectively. However, due to the functional form, the maximum efficiency at $t = 0$ day is 72%, which is in rough agreement with other estimates from R. T. Wollaeger et al. (2018).

3.2.2. Local Thermalization Efficiency Prescription

For the local thermalization prescription, we break down the thermalization efficiency of each component of *r*-process decay products according to the formula presented in J. Barnes et al. (2016), S. Rosswog et al. (2017), and M. Bulla (2023):

$$f_j(\boldsymbol{r}, t) = \frac{\ln(1 + 2\eta^2)}{2\eta^2}, \tag{6}$$

where r is the position in the ejecta, $2\eta^2 = \frac{2A_j}{t\rho(\boldsymbol{r}, t)}$, and A_j is [1.2, 1.3, and 0.2] $\times 10^{-11}$ g cm^{-3} s for alpha particles, beta particles, and fission fragments, respectively, and $f_j(\boldsymbol{r}, t)$ is the equivalent of $f_{\rm tot}$ but as a function of position and for a decay product j. Following M. Bulla (2023), we assume that the radioactive decay products carry 35%, 40%, 20%, 5%, and 0% of the decay energy for neutrinos, gamma-rays, beta particles, alpha particles, and fission fragments, respectively, as supported by the findings of J. Barnes et al. (2016) and R. T. Wollaeger et al. (2018) for the distribution of decay energy.

Neutrinos are assumed to escape immediately and do not contribute to heating the ejecta due to low densities ($\rho \lesssim 10^{-8}$ g cm^{-3} at all times simulated). This implies an instantaneous loss of 35% of *r*-process heating energy at all times and causing a maximum efficiency of 65% at $t = 0$ day. Gamma-rays are simulated directly by injecting them into the zone of *r*-process decay as 1 MeV photons where they can be absorbed or scattered. While a more realistic distribution of gamma-ray energies that emerge from *r*-process decay would improve the accuracy of the simulations, the effect is likely negligible as the difference in energy deposition from gamma-rays of differing energies via Compton scattering is only important in regions of optical depth $\sim$1. Due to the low mass and high speed of typical KN ejecta, the ejecta rapidly becomes optically thin to gamma-rays on the scale of a couple days, limiting the region of optical depth approximately 1% to a few percent of the total ejecta mass and therefore only a few percent of the *r*-process decay energy of which less than half is

comprised of gamma-rays. To confirm this, we ran a comparative KN model in which all gamma-rays were injected as 0.5 MeV photons, which resulted in a higher optical flux by a few percent compared to an identical model injected with only 1 MeV photons.

However, both the global and local thermalization prescriptions are limited by the nature of them being simplified analytical forms to complex nuclear decay chains and interactions. Fully simulating the decay products and corresponding interactions with the surrounding material, while more computationally expensive, would resolve some of the uncertainties in modeling KNe and has been successfully incorporated previously (e.g., K. Hotokezaka & E. Nakar 2020; L. J. Shingles et al. 2023).

4. Kilonova Light Curve and Spectra

We first discuss the impact of atomic data set and thermalization prescription on the observables of a fiducial KN model of $M = 10^{-2}\,M_{\odot}$, $v = 0.1c$, $\log_{10}(X_{\rm lan}) = -2$.

Figure 1 illustrates the differences in light curves caused by the choice of atomic data and thermalization prescription for the fiducial model; despite having the same ejecta parameters, the LSST r and y filters, the JWST F115W, F277W, F560W filters, and bolometric luminosity curves, while initially within $\sim$1 mag of each other, rapidly diverge as the ejecta becomes optically thin. The optical filters, r and y, are strongly impacted by the choice of atomic data for light r-process elements ($31 \leqslant Z \leqslant 50$), as seen by comparing the differences between atomic data sets `HULLAC` and `ATOMIC` (which share light r-process atomic data) against `Autostructure`, similarly to as seen in Figure 3 of L. J. Shingles et al. (2023) when the use of a wavelength-calibrated Sr, Y, and Zr data set resulted in significantly different spectra. The differences in lanthanide atomic data most strongly impact the light curves in the NIR and MIR JWST filters as each atomic data set creates an entirely unique light curve with typical offsets of 4–6 mag by $\delta t \sim 2$ weeks.

The dotted lines and solid lines in Figure 1 represent the global and local thermalization prescriptions, respectively. The thermalization prescription has the greatest impact in optical filters and at early times, with the global prescription increasing the emission by 0.5–1 mag compared to that of the local prescription. The local prescription accounts for the fact that thermalization will be relatively lower in the low-density outer layers of ejecta, from which much of the early emission arises. Eventually, the bolometric luminosity curves of the two prescriptions converge once the ejecta becomes optically thin and the light curves maintain an approximately constant offset as the KN fades.

4.1. Spectra

While the different atomic data sets generate remarkably different light curves, they all agree on the same general spectral features at early times: a doubly peaked spectrum with the bluer peak at $\sim$1 μm and the second at $\sim$1.5 μm (though this may largely be due to the peak blackbody wavelength for temperatures typical of KNe, a few $\times\,10^3$ K, and qualitatively similar high-opacity feature between the peaks) with a rapidly decaying blue flux and a long-lasting red flux. Figure 2 shows a spectral sequence from 2 to 15 days post merger of the fiducial $M = 10^{-2}\,M_{\odot}$, $v = 0.1c$, and $\log_{10}(X_{\rm lan}) = -2$ model using the local thermalization efficiency prescription for each atomic data set.

The differences in line locations and strengths between atomic data sets become most obvious in the late-time spectra as distinct features from lines or line blends emerge. While effects such as NLTE would likely alter the precise shape of the spectra at these late times, the disagreement in the placements of the lines illustrates the level of uncertainty in lanthanide atomic structure. Furthermore, the pattern of lines is qualitatively different; the pattern of features is entirely unique and not mirrors of other models shifted redward or blueward. Extracting information based on locations of spectral features is challenging, even when transitions with experimentally determined wavelengths are matched to spectra (i.e., the explanations of features in AT2017gfo as Sr II from D. Watson et al. 2019 or NLTE He Y. Tarumi et al. 2023, possible Y II from A. Sneppen & D. Watson 2023, Te III from K. Hotokezaka et al. 2023).

4.2. Model Grid Light Curve Properties

Figure 1 clearly demonstrates that each atomic data set results in substantial changes in light curve properties such as peak magnitude and rise time to peak, color, decay rate post peak, and time above half peak luminosity. In the following sections, we use those metrics to quantify the differences between models in more detail by expanding our analysis to the grid of KN models with $M \in [0.001,\ 0.01,\ 0.1]\ M_{\odot}$, $v_k \in [0.1,0.3]\ c$, and $\log_{10}(X_{\rm lan}) \in [-9,\ -4,\ -2]$, to identify the impact of atomic data and thermalization prescription on observational properties and how that impact changes with ejecta properties.

4.2.1. Peak Magnitudes and Peak Times

Figures 3 and 4 show the peak magnitude and time since merger for JWST and LSST filters, respectively, for each model in the grid. We select these filters for their practical and discriminating power; LSST carried out on the Rubin Observatory, if equipped with Target of Opportunity capabilities, has large discovery potential, thanks to the combination of exquisite sensitivity and large field of view (i.e., R. Margutti et al. 2018; I. Andreoni et al. 2022b) and JWST to put forward quantitative expectations of KN brightness for purposes like determining exposure time as well as the capability to constrain atomic data set. For both LSST and JWST, the reddest bands are the brightest and most useful for discriminating between different model parameters. Furthermore, the effects of choice of atomic data set already becomes apparent in the simple observable of time of peak and peak magnitude and especially so at redder filters; for the same ejecta parameters, while the peak magnitude is approximately constant, the time at which the KN achieves its peak shifts by almost four days in the highest $X_{\rm lan}$ models in the reddest JWST filters. Similarly, the choice of thermalization efficiency prescription changes the peak magnitude in most LSST filters by at least a magnitude.

4.2.2. Color

Figure 5 shows the color at the time of peak of the shorter wavelength filter. There is clear correlation of color with ejecta mass, velocity, lanthanide fraction, atomic data set, and thermalization prescription. Higher $X_{\rm lan}$ models produce redder emission, more massive models reach a more luminous peak

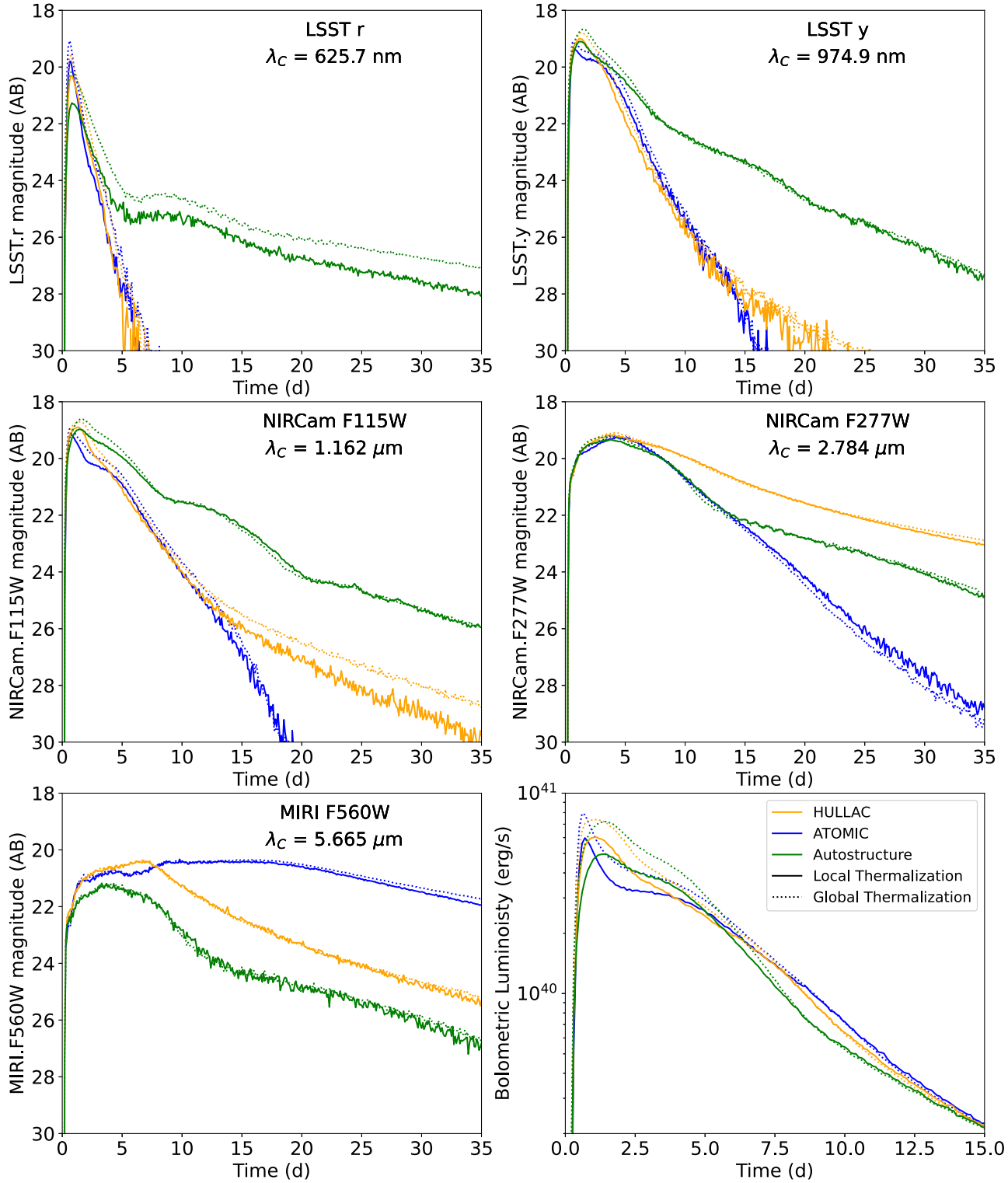

Figure 1. Comparing the fiducial model of $M = 10^{-2}\,M_{\odot}$, $v = 0.1c$, $\log_{10}(X_{\rm lan}) = -2$ across the LSST r and y filters, the JWST F115W, F277W, F560W filters, and bolometric luminosity curve with atomic data sets `HULLAC`, `ATOMIC`, and `Autostructure` in orange, blue, and green, respectively, at a distance of 40.7 Mpc. Models using the local thermalization prescription are solid lines, while the global thermalization prescription is represented by the dotted line. The choice of atomic data for light r-process elements ($31 \leqslant Z \leqslant 50$) has a dramatic impact on optical emission as seen by the differences between atomic data sets `HULLAC` and `ATOMIC` against `Autostructure`. Differences in lanthanide atomic data result in a $\gtrsim$3 mag difference at NIR and MIR wavelengths by $\delta t \sim 2$ weeks that only continues to grow. The global thermalization prescription tends to increase emission across filters by 0.5–1 mag, especially at bluer filters and at early times while the ejecta is optically thick. Notably, we would expect NLTE effects to become important at $\delta t \sim 13$ days as per Equation (3).

magnitude, and models with higher characteristic velocities achieve similar or bluer colors than their slower counterparts. Effectively, each mass of the model grid forms arcs in the color-peak-magnitude space where the mass sets the starting point along the peak-magnitude axis and the $X_{\rm lan}$ determines where along the arc the model sits. Choice of atomic data set

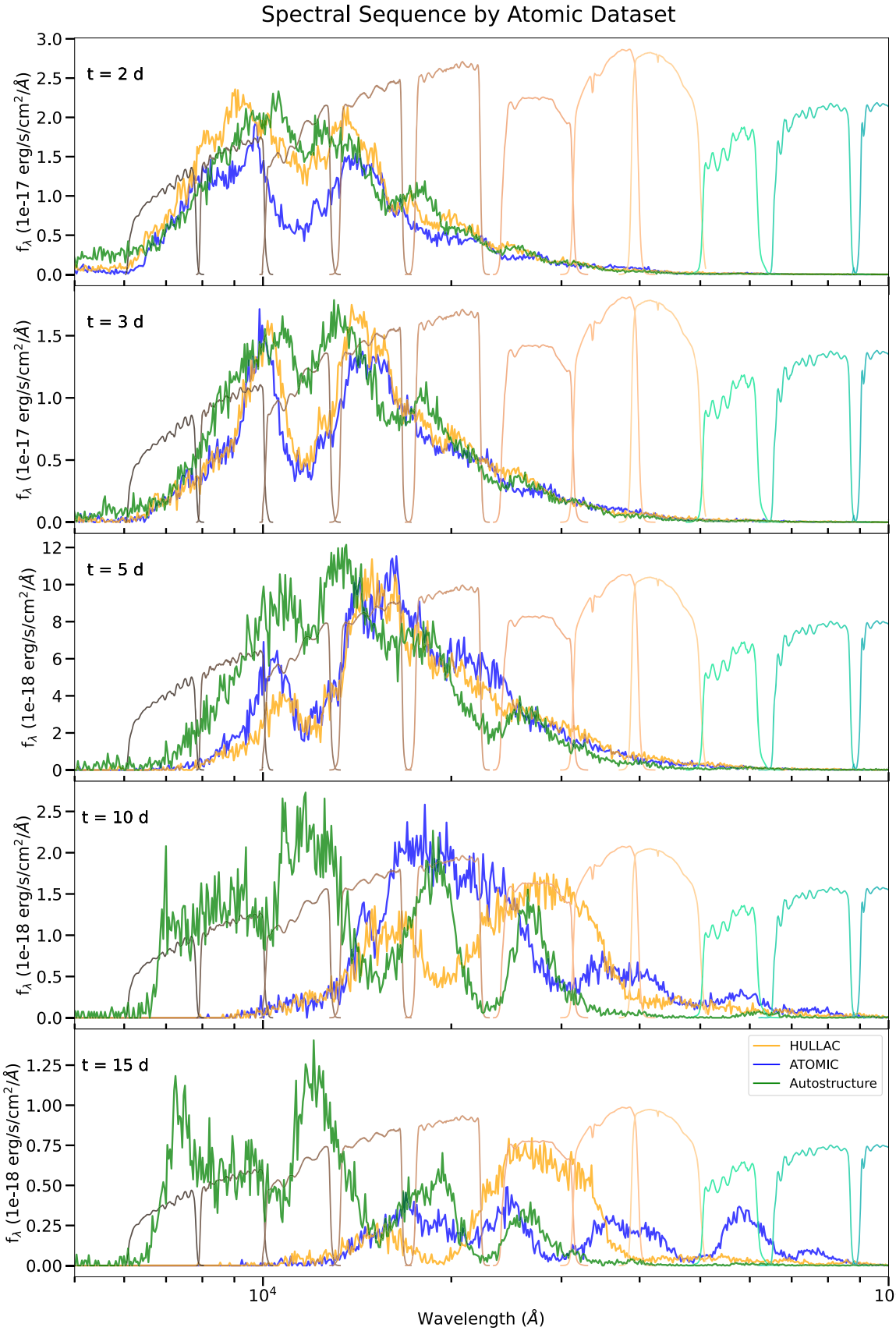

Figure 2. Spectral sequence of a $M = 10^{-2} M_{\odot}$, $v = 0.1c$, $\log_{10}(X_{\rm lan}) = -2$ model using atomic data set `HULLAC` (orange), `ATOMIC` (blue), and `Autostructure` (green) at $t = 2$, 3, 5, 10, and 15 days overlaid on top of the transmission curves of JWST photometric filters. At early times, the predictions from each atomic data set agree relatively well, but rapidly diverge (particularly in the IR) and result in vastly different colors. The $\delta t = 15$ days spectral comparison, while likely in a regime where NLTE will affect the precise shape of features, particularly shows the uncertainty in the specific locations of lines between atomic data sets from the qualitative differences in shape, which should remain unaffected by NLTE effects.

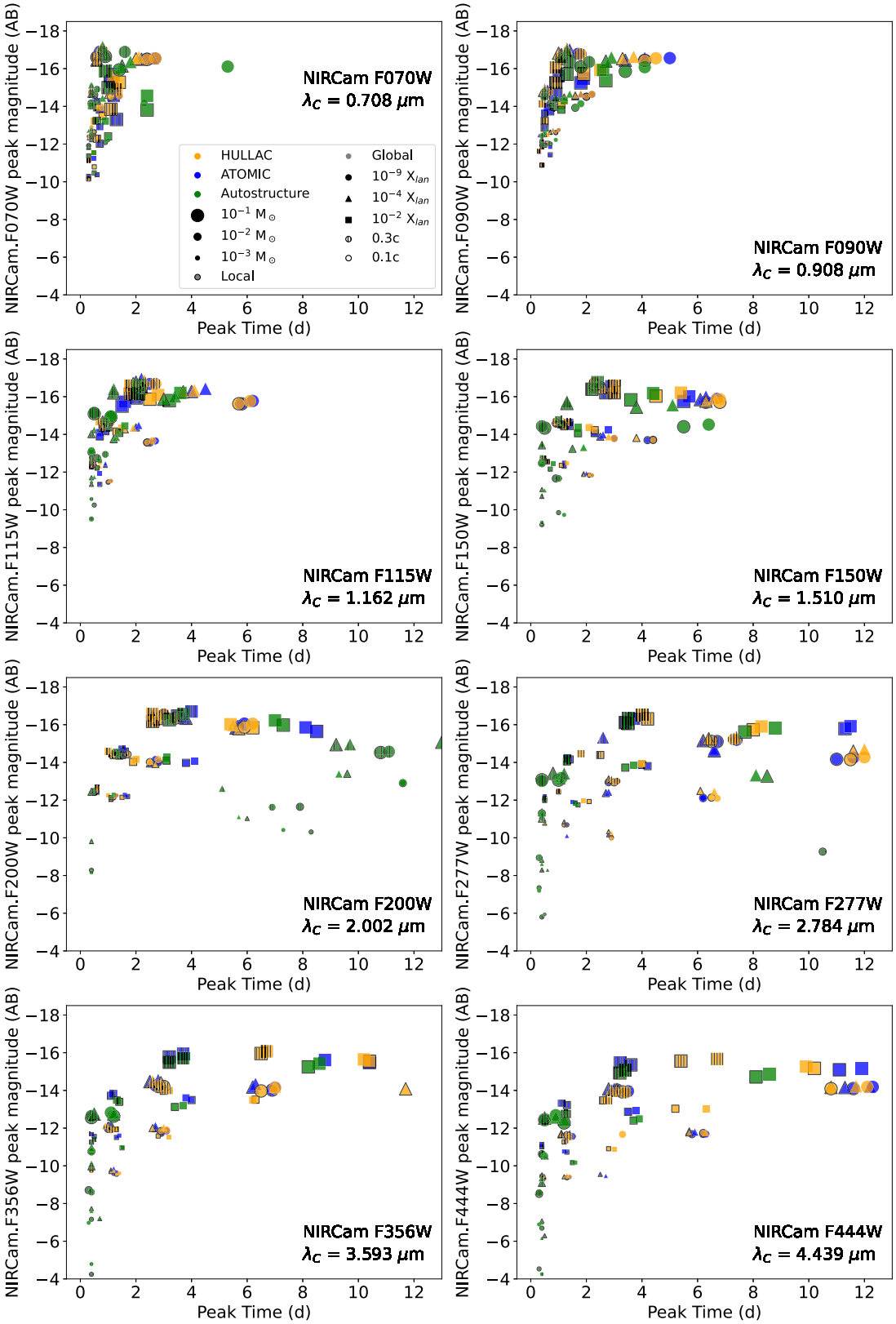

Figure 3. Parameter space for peak absolute magnitude in each JWST NIRCam filter vs. peak time. Models using atomic data set `HULLAC` are in orange, data set `ATOMIC` in blue, and data set `Autostructure` in green. Larger size corresponds to larger mass models. A black outline indicates that the local thermalization efficiency prescription was used, while no boundary indicates global thermalization prescription. Circles, triangles, and squares indicate $\log_{10} X_{\rm lan} = -9$, -4, and -2, respectively. Hatches inside the markers indicate a model with characteristic velocity of $0.3c$, while those without indicate $0.1c$. The effects of choice of atomic data set already becomes apparent in the simple observable of time of peak and peak magnitude and especially so at redder filters; for the same ejecta parameters, while the peak magnitude is approximately constant, the time at which the KN achieves its peak shifts by almost four days in the highest $X_{\rm lan}$ models in the reddest filters.

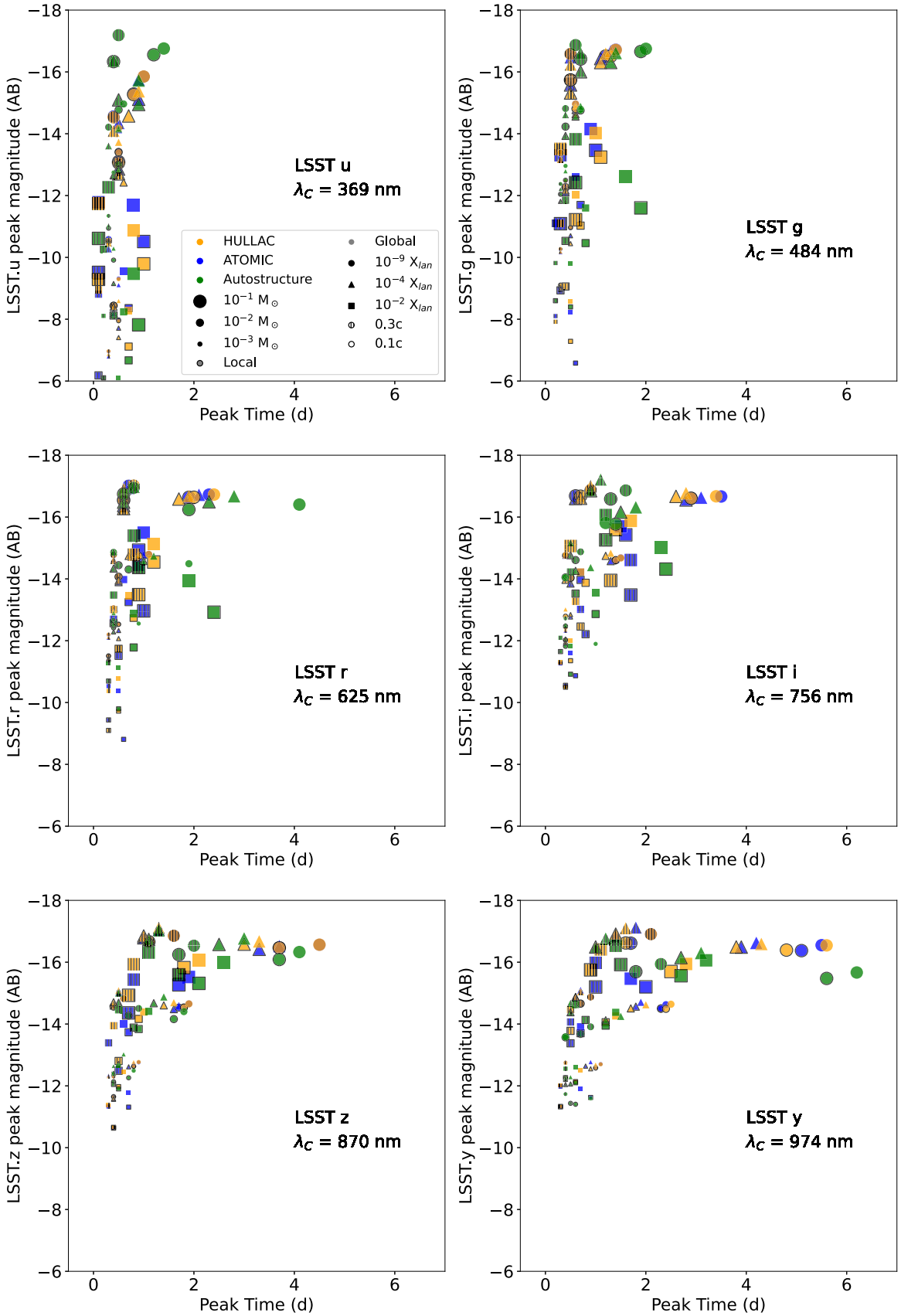

Figure 4. Same as Figure 3, except for each LSST filter *u*, *g*, *r*, *i*, *z*, and *y*. Similarly to the JWST filters, the reddest filters show the largest spread in days until peak among the different atomic data sets. As many of the LSST filters are blueward of JWST, this highlights the rapid decline of KNe at blue wavelengths as the majority of models achieve their peak in the *u*, *g*, and *r* filters within two days of merger.

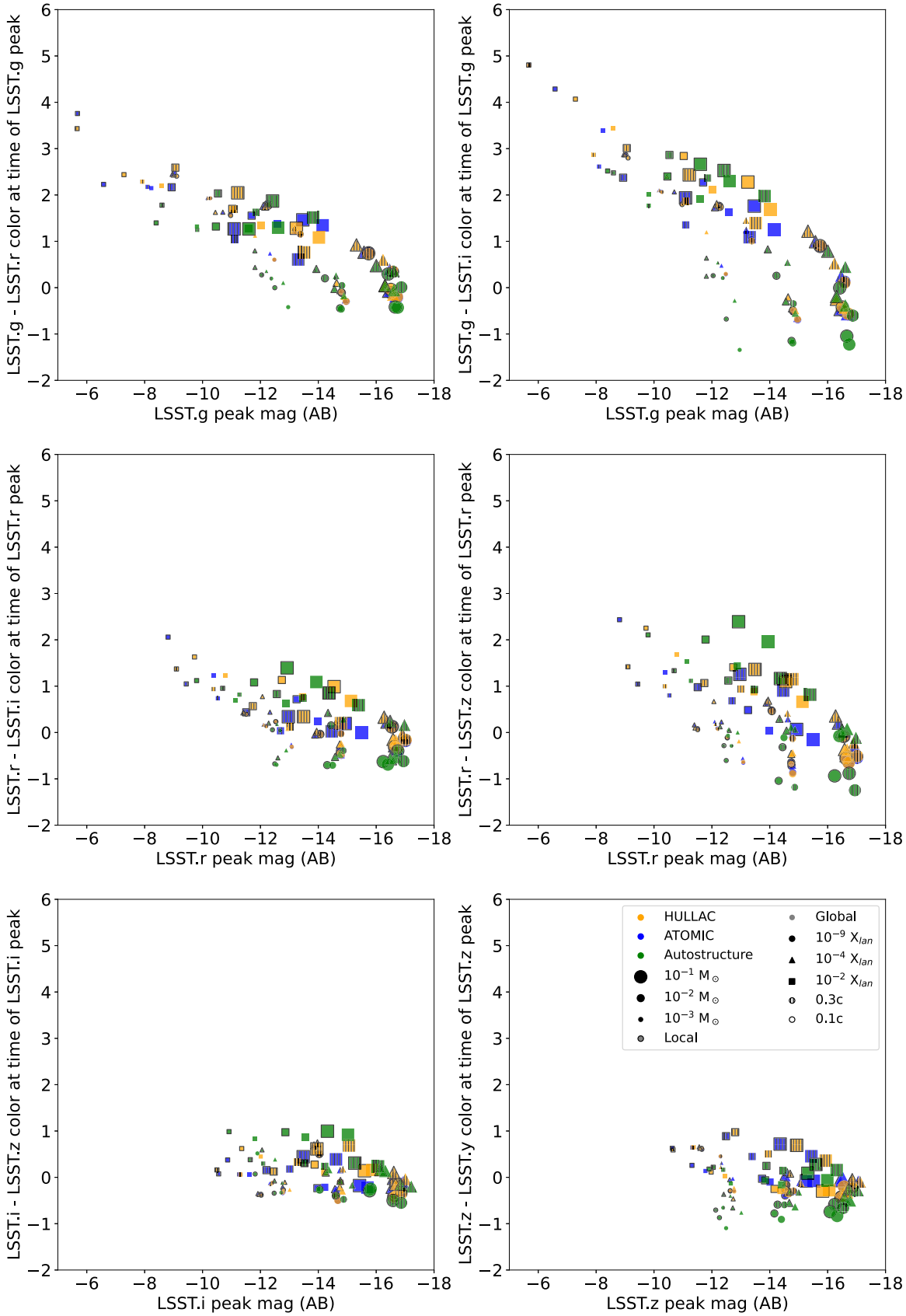

Figure 5. Same legend as Figure 4. Parameter space of LSST $g-r$, $g-i$, $r-i$, $r-z$, $i-z$, and $z-y$ color at time of peak of the first filter. Due to the spacing of the grid, it is possible to see that each unique mass forms an arc of models in this parameter space, with more massive models pushing to higher peak magnitudes and higher $X_{\rm lan}$ pushing models to redder colors and fainter peak magnitudes, creating an observable arc.

sits at what color value the arc ends, with atomic data set ATOMIC models generally ending at the reddest colors for the highest $X_{\rm lan}$ models. As a second-order effect, the choice in thermalization efficiency prescription shifts the KN along the arc with the global prescription resulting in a bluer KN and the local prescription a redder KN. The farther apart the filters are in wavelength space, the easier it becomes to distinguish KN ejecta parameters based on where they fall in this parameter space. However, observational limitations such as limiting magnitudes will place constraints on the feasibility of sampling maximally wavelength separated colors like $g-y$, and so colors with smaller wavelength separation like $g-z$ may prove more fruitful.

4.2.3. Decay Rate and Time Above Half Peak Luminosity

Figure 6 shows the rise rate in magnitudes per day in each LSST filter as a function of magnitude at $t=t_{\rm peak}+2$ days. Bluer filters like u, g, and r are much more rapidly decaying than redder filters like i, z, and y with some models having minimal decay. The light curves resulting from the atomic data sets begin to diverge in characteristics with atomic data set Autostructure models as the slowest declining in the bluest filters while light curves from atomic data set ATOMIC models tend to be more rapidly declining and therefore redder than the light curves of other atomic data sets, though the divergence is not sufficient to distinguish between atomic data sets HULLAC and ATOMIC by decay rate alone.

Figure 7 shows the time spent in each filter above half the peak luminosity. The emission in bluer filters rarely lasts more than a few days above half maximum while the emission in red filters can spend more than a week above half maximum. The emission from atomic data set Autostructure models stands out due to the longer times above half peak across all filters by up to a factor of 2 as a result of the slower decay rate.

4.2.4. Bolometric Luminosity

Figure 8 shows the ratio of the bolometric luminosity curves of the global to the local thermalization efficiency prescriptions. The ratio has been smoothed then rescaled by a factor of 0.65/0.72 to correct for the disagreement in maximum efficiency to ensure that any differences are due to the intrinsic analytical formulae instead of a disagreement about the assumed fraction of decay energy that escapes in neutrinos. There is a clear difference in luminosity of factors between 0.8 and ∼1.5 that evolve with time. This indicates that the two thermalization prescriptions deposit a substantially different amount of r-process decay energy in the ejecta, leading to discrepancies in the bolometric luminosity.

Choice of atomic data set largely affects the shape of the bolometric luminosity curve, as shown in the bottom right panel of Figure 1. The fiducial atomic data set ATOMIC model has a higher opacity and therefore traps more energy at early times, resulting in a lower bolometric luminosity. The energy then emerges at late times as the ejecta becomes optically thin, which creates the brighter late-time bolometric luminosity curve than the models using atomic data sets HULLAC and Autostructure.

4.3. Atomic Data Systematic Uncertainty

The above figures show that the different atomic data sets produce a range of KN colors for the same ejecta properties, with atomic data set Autostructure producing the bluest, atomic data set ATOMIC producing the reddest, and atomic data set HULLAC being in between the two. At smaller $X_{\rm lan}$, the differences between atomic data sets HULLAC and ATOMIC are minimal, as expected since they share nonlanthanide atomic data, but are substantial for the highest $X_{\rm lan}$ models where lanthanide opacities dominate. For example, the highest $X_{\rm lan}$ and most massive models exhibit a scatter of almost 3 mag in the u band while peaking at approximately the same time, while in the y band, the scatter shrinks to less than a magnitude in brightness and approximately a day in peak time (Figure 4).

The scatter of observational properties within an atomic data set is typically quite similar, though offset from one another. The offset for each atomic data set is most prominent in the colors of each model (Figure 5), namely the $g-i$, $r-i$, and $r-z$ colors that span between 1.5 and 2 mag difference in colors for the highest $X_{\rm lan}$ models. This is also true of the decay rate in each LSST filter, especially the bluest filters (Figure 6). Many of the models with atomic data sets HULLAC and ATOMIC so rapidly decay in the u band that most models have dropped by more than 5 mag in a day, while atomic data set Autostructure models are declining much more slowly at $\sim$1.5 mag day^{-1}. The substantial difference in atomic data means that the bluest filter that achieves a scatter across atomic data sets of decay rate of less than $\pm$0.1 mag day^{-1} is the z band, though this is likely due to the fact that the overall extent of the color and decay rate phase space covered by the models shrinks when looking at redder filters. The spread between atomic data sets only grows for lower mass models, with a spread of z-band decay rate of approximately 1 mag day^{-1}.

Therefore there is a tension in determining the optimal filter for discerning KN ejecta properties; bluer optical filters like u, g, and r have a higher intrinsic spread that can be utilized to identify ejecta properties but are the most model dependent. Redder optical filters like i, z, and y are less model dependent but have a lower intrinsic spread and are more difficult to discern ejecta properties.

At late times, the difference between atomic data sets is most apparent in the IR colors. In Figure 2, the remaining features at 15 days dominate the predicted colors for each model, and their different placements manifest as vastly different colors. Atomic data set HULLAC is dominated by a feature at $\sim$2.5 μm, while atomic data set Autostructure has a number of features spanning most JWST NIR filters. Atomic data set ATOMIC is the only data set to have a long-lasting MIRI feature, resulting in an extremely long-lived MIRI light curve and red color. However, we caution using the LTE models presented here, as line lists are incomplete for MIR wavelengths and the nebular MIR spectra may be able to resolve individual atomic lines.

4.4. Thermalization Efficiency Systematic Uncertainty

The impact of thermalization prescription on observational properties manifests as a systematic offset in a direction that mimics more massive models across all atomic data sets and ejecta parameters. For example, in Figures 3 and 4, the global thermalization prescription drives points to brighter and later peaks. Similarly, the global thermalization prescription pushes a given KN to brighter and bluer colors in Figure 5.

Figure 8 shows the systematic brightness offset of the global thermalization-prescription models compared to the local thermalization-prescription models. Luminosity is most tightly correlated with the ejecta mass through the r-process heating

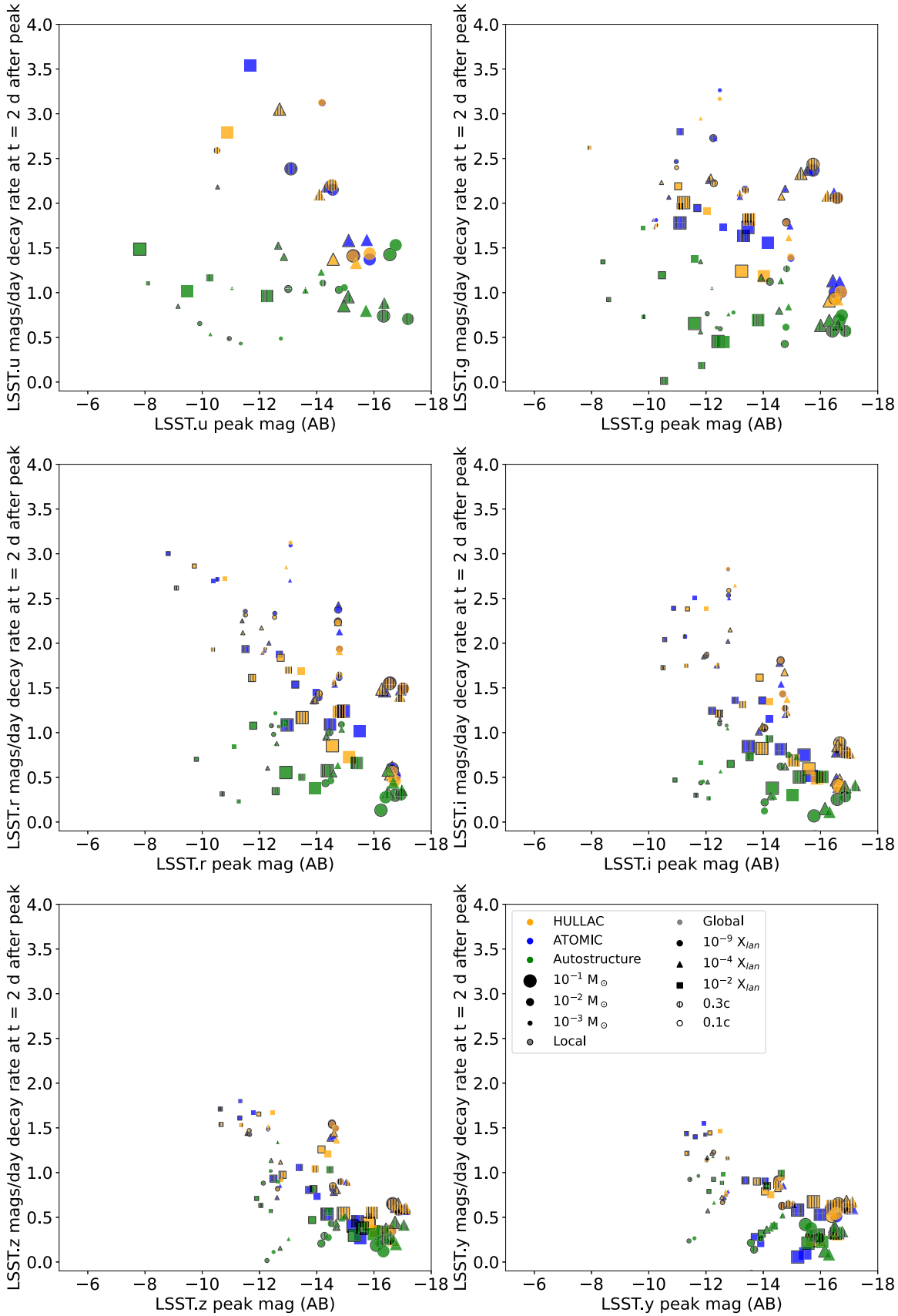

Figure 6. Parameter space of the decay rate in each LSST filter vs. the magnitude at $\delta t = 2$ days after peak of a given filter. Atomic data set `Autostructure` stands out as the slowest declining across all LSST filters, especially the bluest filters like *u*, *g*, and *r*.

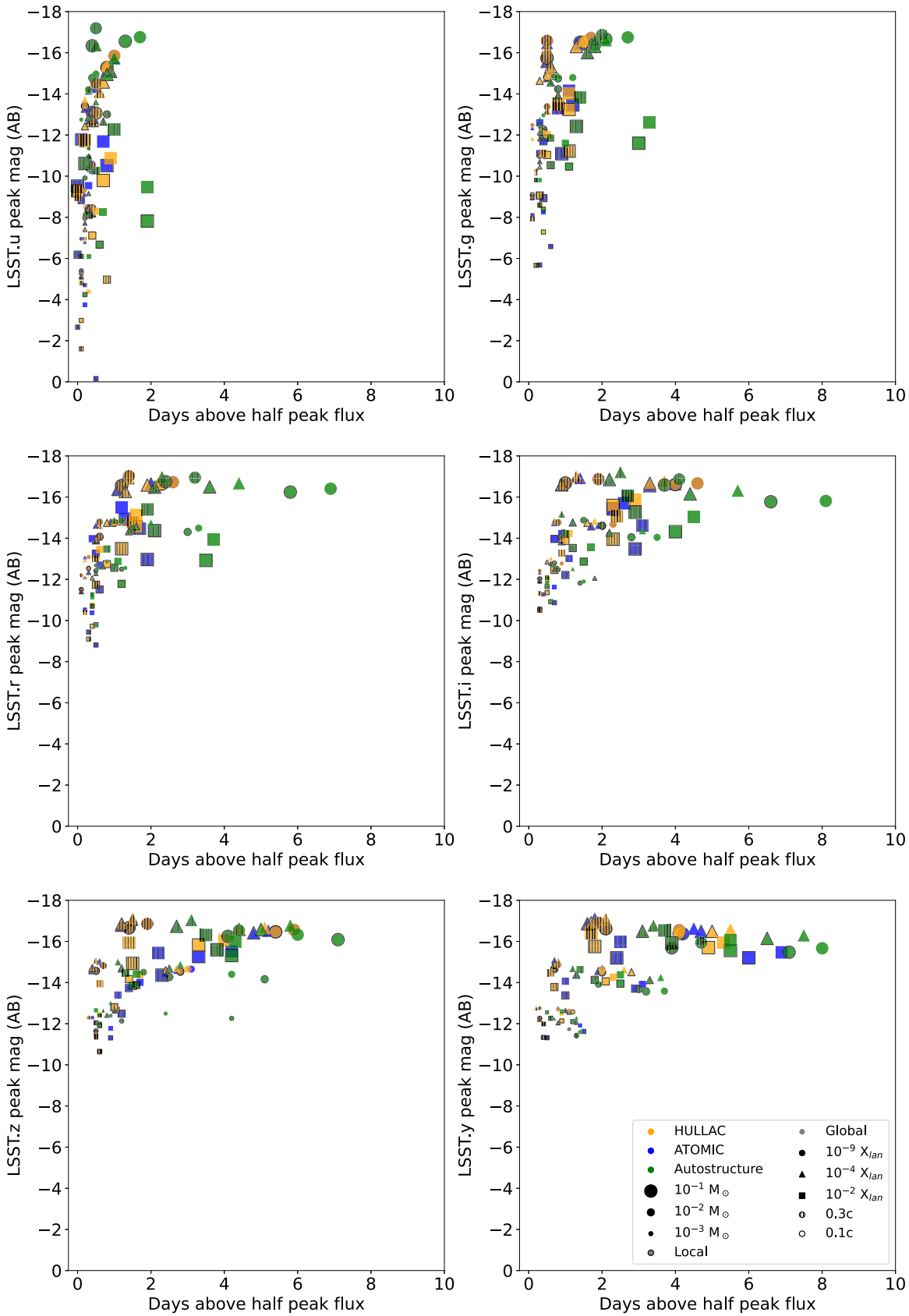

Figure 7. Parameter space of time above half peak vs. the peak magnitude of that filter. Due to the slower decay rate in LSST filters of atomic data set `Autostructure`, those models last above half maximum luminosity by as much as a factor of 2 longer.

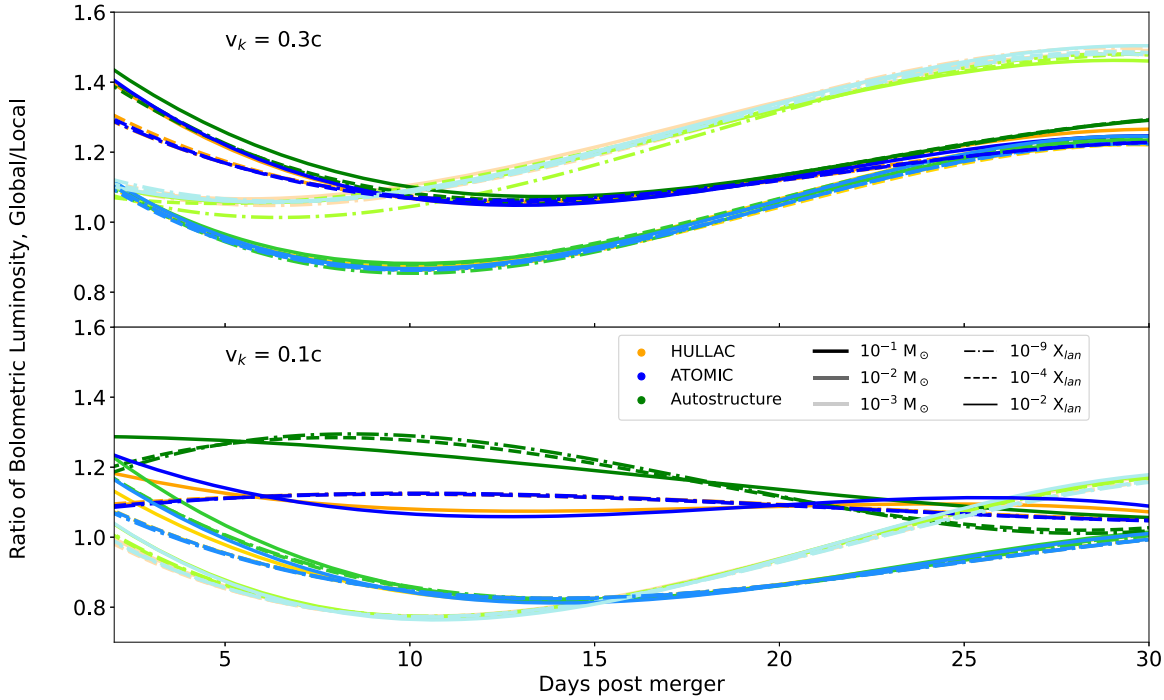

Figure 8. Ratio of the global thermalization-prescription bolometric luminosity to the local thermalization-prescription bolometric luminosity curve as a function of time for each model (smoothed to remove numerical noise) with $v_k = 0.3c$ models in the upper panel and $v_k = 0.1c$ models in the lower panel, and lighter colors representing smaller masses. The predictions from global prescription models tend to differ from the local prescription predictions by ∼20%–50%. Excluding the least massive models limits the offset to up to ∼30%, regardless of atomic data set and $X_{\rm lan}$.

rate, as an increase in mass results in an increase in *r*-process decay energy. The effect of thermalization efficiency prescription on inferring the correct velocity measurement is negligible, as it largely affects the overall normalization of the spectra at each epoch.

Roughly, the 20%–50% offset in luminosity can correspond to a difference in ejecta mass estimation of those factors. More massive models appear to be less affected, with uncertainties up to ∼30%. This may be because the more massive models remain optically thick for longer and the fraction of energy lost by the outermost ejecta is more negligible compared to that of the less massive models. Figure 8 additionally makes clear that this systematic difference happens regardless of atomic data as models with the same ejecta parameters eventually converge. This is to be expected, as at early times when the ejecta is optically thick and blackbody-like the difference in spectra is a result of differing strong absorption features that allow a varying luminosity to escape. As the ejecta becomes optically thin, the luminosity of the KN becomes approximately the *r*-process heating rate as all radiation can instantly escape the ejecta and so becomes the same across all models regardless of atomic data set. Thus, the difference in luminosity between the models reflects the underlying difference in thermalization factors.

From Figures 3–8, it becomes immediately clear that treating the thermalization efficiency prescription globally as opposed to locally causes a systematic offset in model observable properties approximately in the same direction across all atomic data sets, masses, velocities, and lanthanide fractions for each observable property. Generally, the global thermalization efficiency prescription retains more energy in the ejecta than the local thermalization efficiency prescription, resulting in brighter KNe across all wavelengths, though especially at optical wavelengths. Additionally, using a local thermalization efficiency prescription allows for more accurate modeling of ejecta structures beyond those used in the numerical calculations of J. Barnes et al. (2016).

5. Effects on Parameter Estimation

The previous sections have shown that choices of atomic data and thermalization prescription can lead to large systematic offsets in observable properties and therefore in the estimation of KN parameters. Here, we quantify the systematic uncertainty due to thermalization efficiency prescription and atomic data set.

In the era of LSST, there may be serendipitous discoveries of KNe that are only discovered well after the transient has faded. In these cases, the limited LSST data set collected can still constrain valuable ejecta properties based on the characteristics of the light curve (e.g., P. S. Cowperthwaite et al. 2019; I. Andreoni et al. 2022a). In the following sections, we discuss the impact the various atomic data sets and thermalization prescription may have on parameter estimation for cases in which there may only be a handful of photometric points across a few bands.

5.1. Error Estimation with GW170817

To illustrate the impact of the systematic uncertainty caused by atomic data, we refit GW170817/AT2017gfo to derive properties of the ejecta using each atomic data set. We fit the light curves by adding together two 1D models, a low $X_{\rm lan}$ component and a high $X_{\rm lan}$ component to mimic the polar, blue ejecta and the red, dynamical ejecta interpretation of ejecta components. While summing the emission does not take into account effects of interaction between the two components, it is sufficient to quantify the difference in parameter estimation between the various atomic data sets and commonly used in

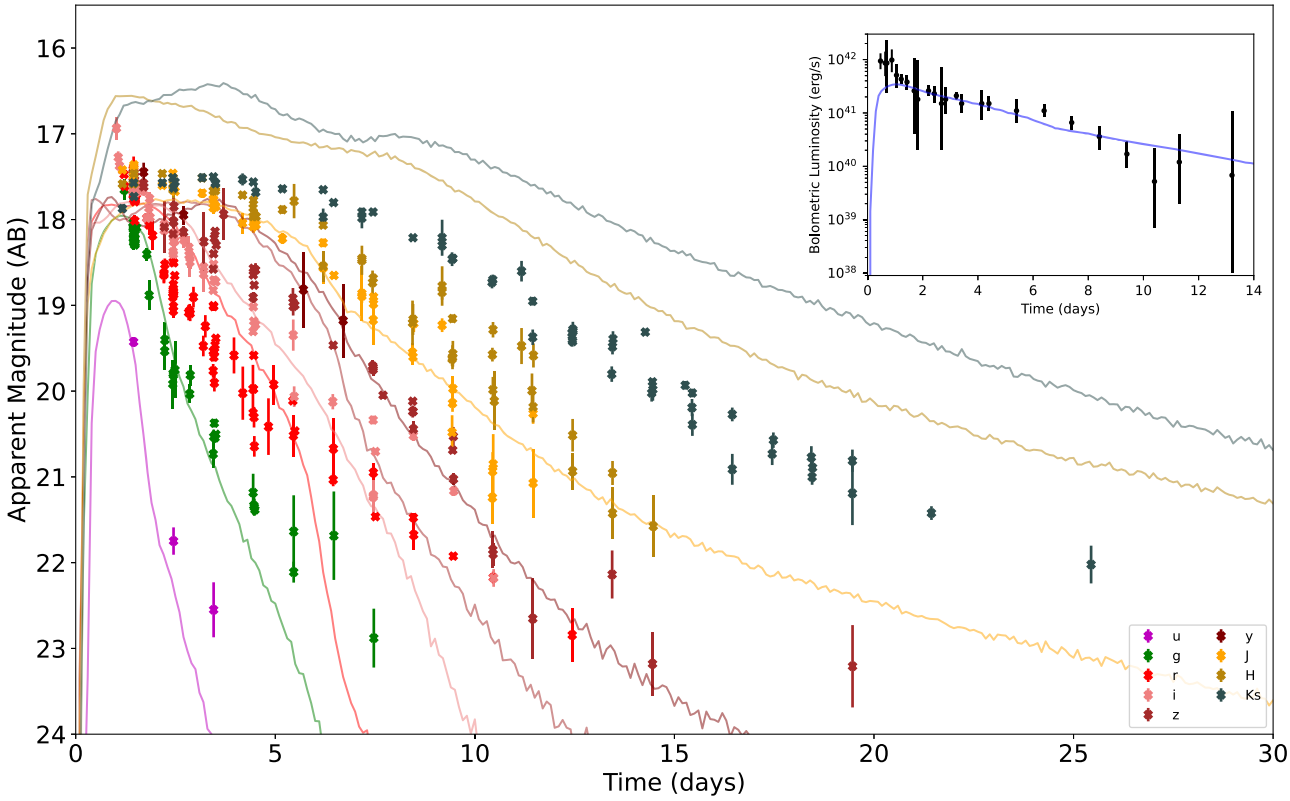

Figure 9. Best-fitting light curve model for atomic data set HULLAC with bolometric luminosity points from M. W. Coughlin et al. (2018) and model bolometric luminosity in the inset. M. W. Coughlin et al. (2018) extrapolates the SED to redward of 2.5 μm by fitting a blackbody to photometric points, which tends to overestimate the true bolometric luminosities of the models presented in this work. The model tends to underproduce optical flux until z band, agree for J band, then overproduce H and Ks bands while having a similar bolometric luminosity. This is likely indicative of too much reprocessing of optical light into IR and demonstrates the difficulty of simplified 1D models fitting AT2017gfo.

other analyses (i.e., M. W. Coughlin et al. 2018). We present these "fits" as relative estimates to capture the systematic error between atomic data sets, not as absolute fits with statements about the true parameters of GW170817.

We use a grid with masses $M \in [0.01, 0.02, 0.03, 0.04, 0.05]\ M_{\odot}$, $v_k \in [0.05, 0.1, 0.2, 0.3]\ c$, and $\log_{10}(X_{\rm lan}) \in [-9, -5, -4, -3, -2]$ as components for each model. Additionally, we include the models described in Section 2 for model-matching purposes. We fit the light curve of g, r, i, z, y, J, H, and Ks filters presented in V. A. Villar et al. (2017) and references therein at times $\delta t \geqslant 1$ day to the equivalent LSST and 2MASS filters by minimizing the weighted χ^2 function

$$\chi^2 = \sum_i^N \frac{w_{{\rm obs},\,i}^2 (y_{{\rm obs},\,i} - y_{\rm m})^2}{\sigma_{\rm m}^2}, \tag{7}$$

where $w_{\rm obs}$, $y_{\rm obs}$, $y_{\rm m}$, and $\sigma_{\rm obs}$ are the weights, observed magnitude, model magnitude, and observed uncertainty, respectively, and N is the number of observations. Once the best-fitting model within the grid was identified, we then iteratively tested a finer resolution grid around the lanthanide-rich component. At each step, we generated 16 more models that were half the logarithmic distance in $X_{\rm lan}$, half the linear distance in mass, and half the linear distance in velocity to the surrounding grid points.

However, since we use the equivalent LSST or 2MASS filter to compare our models to GW170817, there are two additional error sources that are not included in the photometric data provided by V. A. Villar et al. (2017): the systematic offset of the LSST or 2MASS filter against the similar filter of the observation and the scatter of points caused by the subtle differences in filters across the telescopes used to observe GW170817. As such, we artificially inflate the uncertainties of each observation by a factor equal to the scatter of observed magnitudes across each filter to account for the extra variance of the data set. We then weight each point by dividing by the number of data points with that filter to normalize such that each filter holds an equal weight on the fit and prevent filters with a large number of data points from dominating the fit.

The best-fitting model-matching parameters for each atomic data set are listed in Table 1, and shown in Figures 9, 10, and 11. Importantly, the errors provided in Table 1 are representative of the spacing of the grid and do not reflect the true statistical uncertainties of fitting the AT2017gfo data set; the errors are provided to represent our coarse grid and of the meaningfulness of the difference in parameter estimates between the atomic data sets.

The best-fitting models using atomic data sets HULLAC and ATOMIC are overluminous in the H and Ks bands while tending to be slightly underluminous in optical bands (Figures 9, 10, and 11). However, the bolometric luminosity (shown in the upper right corner of each Figure as calculated by M. W. Coughlin et al. 2018 with the bolometric luminosity of the model in blue) is approximately correct. Taken together, one explanation is that this indicates these models produce approximately the correct luminosity but reprocess too much of the optical emission into the IR. Additionally, atomic data sets HULLAC and ATOMIC have a long-lasting feature that aligns with the H and Ks filters

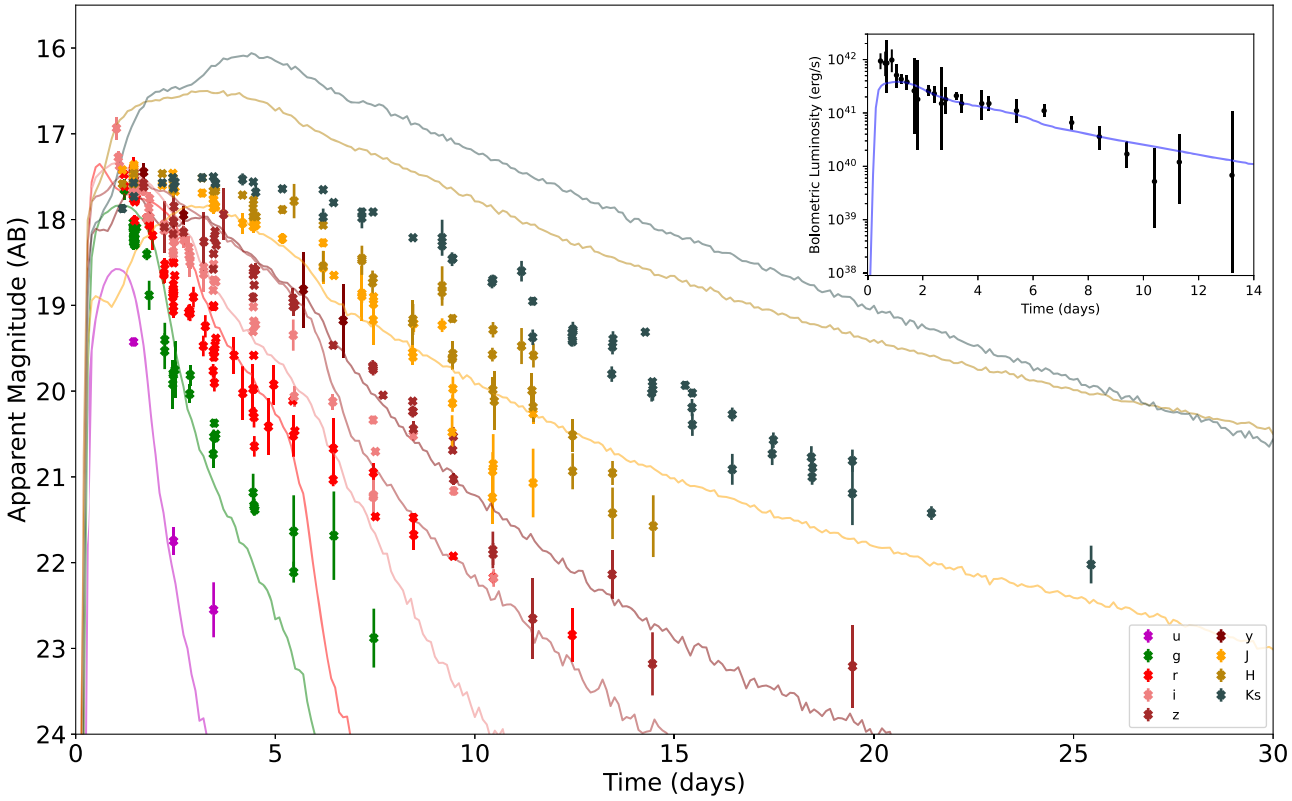

Figure 10. Best-fitting light curve model for atomic data set ATOMIC. Similarly to Figure 9, ATOMIC overproduces *H* and *Ks* bands while underproducing optical emission, especially at $\delta t \gtrsim 5$ days, though the bolometric luminosity curve is consistent.

Table 1
"Best-fitting" Model-matching Ejecta Parameters from our χ^2 Fitting of GW170817 Data

Data Set	M_1 ($10^{-2}\,M_\odot$)	v_1 (c)	$\log_{10}X_{\rm lan1}$	M_2 ($10^{-2}\,M_\odot$)	v_2 (c)	$\log_{10}X_{\rm lan2}$	Total Lanthanide Mass ($M_\odot$)	χ^2
HULLAC	$2.5^{+0.13}_{-0.13}$	$0.05^{+0.01}_{-0.01}$	$-3.25^{+0.13}_{-0.13}$	$1.5^{+0.13}_{-0.13}$	$0.3^{+0.025}_{-0.025}$	-9^{+2}_{-2}	1.5×10^{-5}	1.12
ATOMIC	$2^{+0.13}_{-0.13}$	$0.05^{+0.01}_{-0.01}$	$-3.75^{+0.13}_{-0.13}$	$2^{+0.13}_{-0.13}$	$0.2^{+0.013}_{-0.013}$	-9^{+2}_{-2}	4×10^{-6}	1.26
Autostructure	$2^{+0.13}_{-0.13}$	$0.05^{+0.01}_{-0.01}$	$-3^{+0.13}_{-0.13}$	$2^{+0.5}_{-0.5}$	$0.3^{+0.05}_{-0.05}$	$-4^{+0.5}_{-0.5}$	2.2×10^{-5}	0.319

Note. Uncertainties are based on grid spacing.

but has a steep decline in flux just blueward the *J* filter, causing the large color difference that does not exist in atomic data set Autostructure models.

However, the large IR output is needed to achieve the late-time IR color observed in GW170817. M. M. Kasliwal et al. (2022) present Spitzer IR photometric points and limits at $\delta t = 43$ and 74 days for 3.6 and 4.5 μm. While we recommend caution when extrapolating the LTE models presented in this work to such late times, the data presented in M. M. Kasliwal et al. (2022) can help to constrain models. At $\delta t = 43$ days, GW170817 has a 3.6–4.5 μm color of >1.3 mag. By $\delta t = 74$ days, the same color is > -0.8 mag. While high $X_{\rm lan}$ and high mass models using atomic data sets HULLAC and ATOMIC are capable of achieving the brightness of the 4.5 μm photometry point, the $\delta t = 43$ days minimal color is more constraining and only achieved by models using atomic data set ATOMIC under LTE assumptions in the equivalent JWST filters. While effects like NLTE, including actinides or super-heavy elements, or late-time enhanced heating rate from ^{254}Cf (E. M. Holmbeck et al. 2023) that are not included in these models will likely alter these colors, the color evolution provides an ideal avenue to constrain atomic data and abundances.

This is in sharp contrast to even the most massive ($M = 0.1\,M_\odot$) and lanthanide-rich ($\log_{10}(X_{\rm lan}) = -2$) models using atomic data set Autostructure, which are insufficiently bright at 4.5 μm by approximately 4 mag. NLTE radiative transfer will be critical to accurately modeling the color evolution out to such late times and has the potential to meaningfully constrain the atomic data of heavy metals. This has already been done with some success, as K. Hotokezaka et al. (2022) identified a handful of candidate species capable of producing the bright 4.5 μm flux without 3.6 μm flux such as Se III, W III, Os III, Rh II, Rh III, and Ce IV using experimentally identified lines in the NIST database. Interestingly, the lack of a similar 4.5–3.6 μm color in the KN candidate associated with GRB 230307A (A. J. Levan et al. 2024) could be indicative of substantial composition differences among KNe and have implications for galactic *r*-process nucleosynthesis.

The inability of the models presented here to reproduce the IR light curve of AT2017gfo points to a tension in KN

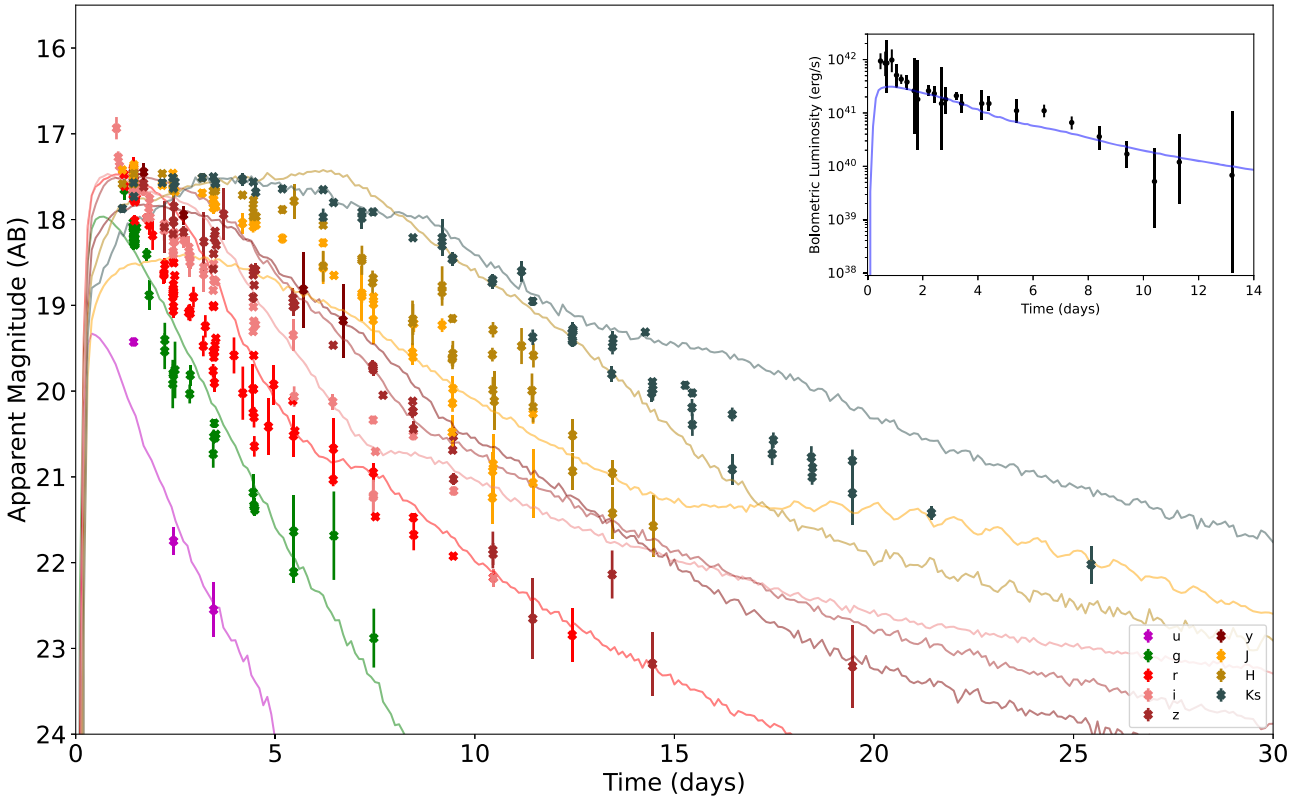

Figure 11. Best-fitting light curve model for atomic data set `Autostructure`. atomic data set `Autostructure` is the only data set presented here that was capable of producing sufficiently long-lasting optical bands and not over-producing IR filters by more than a magnitude at early times, likely due to its treatment of light *r*-process elements.

modeling where it is necessary to produce a bright enough IR transient at late times, but not so bright that the early-time IR is overproduced. There are multiple possible avenues through which this issue could be resolved, including a radial gradient of $X_{\rm lan}$, NLTE effects, a more realistic 3D ejecta structure, or variations in *r*-process heating. Critically, this tension indicates that, with idealized 1D models, there is no atomic data set that will perfectly fit the data.

Table 1 shows that the parameter most impacted by changing atomic data sets is the heavy-metal content of the ejecta; the estimates range from the smallest amount of heavy metals using atomic data set `ATOMIC` ($4 \times 10^{-6}\,M_{\odot}$) to the most with atomic data set `Autostructure` ($2.2 \times 10^{-5}\,M_{\odot}$), differing by a factor of ~6. Despite this high level of variance in lanthanide mass between models, the bolometric luminosity is well approximated by the models at $\delta t \gtrsim 1$ day. The lanthanide-rich component varies by ∼0.75 orders of magnitude while the lanthanide-poor component can vary much more substantially by 5 orders of magnitude. However, at such low $X_{\rm lan}$, the models are largely insensitive to changes until $\log_{10}(X_{\rm lan}) \sim -4$ as the lanthanide bound–bound opacities become subdominant, which is likely the cause of such large uncertainty.

Mass and velocity are less impacted by changes in atomic data set, with agreement among the models within $\pm 0.005\,M_{\odot}$ and velocity within $\pm 0.1c$. Total mass is even less impacted across the atomic data sets, as it remains constant across all "best-fitting" models. The overall level of agreement in mass and velocity may be a result of optical filters dominating the fit, as there were five optical filters and only three IR filters.

5.1.1. Comparison to Other Works

While we stress that our fitting methods are based on model matching and are meant to quantify the error caused by thermalization efficiency prescription and atomic data, it is nonetheless helpful to place the derived numbers in context of those already found for AT2017gfo.

We consider three different estimates of the parameters from AT2017gfo, listed in Table 2, from V. A. Villar et al. (2017), M. W. Coughlin et al. (2018), and M. Ristić et al. (2023). The "fits" presented in this work most closely resemble the estimations of M. W. Coughlin et al. (2018), with most parameters agreeing within $\sim 1\sigma$, though the estimates of M. W. Coughlin et al. (2018) are often larger. This is to be expected as there are many similarities between the process that went into fitting the light curves; M. W. Coughlin et al. (2018) used the models from D. Kasen et al. (2017) in their fitting process, which used atomic data set `Autostructure` and is the closest in agreement. To represent a two-component KN, M. W. Coughlin et al. (2018) also summed two 1D models. The slight disagreement in $X_{\rm lan}$ and $<1\sigma$ mass larger estimate may also be a result of differences in composition, where the D. Kasen et al. (2017) models that M. W. Coughlin et al. (2018) use had a flat distribution of nonlanthanide material, as opposed to the solar abundance distribution used in the models presented here. Notably, the errors on each parameter derived in M. W. Coughlin et al. (2018) also most closely match those presented in this work and are larger than errors presented in many other works. This is a result of the M. W. Coughlin et al. (2018) incorporating a 1 mag uncertainty into their model

Table 2
"Best-fitting" Ejecta Parameters from the Literature of GW170817 Data with 1σ Errors

Source	M_1 ($10^{-2}\,M_\odot$)	v_1 (c)	$\log_{10}X_{\rm lan1}$	M_2 ($10^{-2}\,M_\odot$)	v_2 (c)	$\log_{10}X_{\rm lan2}$
M. W. Coughlin et al. (2018)—Light Curve	$3.09^{+1.63}_{-1.92}$	$0.1^{+0.08}_{-0.06}$	$-1.61^{+0.96}_{-1.04}$	$2.57^{+0.95}_{-1.07}$	$0.17^{+0.09}_{-0.1}$	$-4.73^{+0.41}_{-0.2}$
V. A. Villar et al. (2017)—2 Component	$5^{+0.1}_{-0.1}$	$0.149^{+0.001}_{-0.002}$	$\kappa = 3.65^{+0.09}_{-0.28}$ cm^2 g^{-1}	$2.3^{+0.5}_{-0.1}$	$0.256^{+0.005}_{-0.002}$	$\kappa^{a} = 0.5$ cm^2 g^{-1}
M. Ristić et al. (2023)—Weighted	$1.91^{+0.3}_{-0.3}$	$0.2^{+0.01}_{-0.01}$	-1.28^{a}	$1.58^{+0.3}_{-0.5}$	$0.13\ ^{+0.04}_{-0.04}$	$-\infty^{a}$

Note.
[a] Quantity was fixed in modeling.

fitting and represent one way to proceed with modeling systematic model uncertainties.

M. Ristić et al. (2023) uses models produced with atomic data set ATOMIC for their fitting process, and imposes a fixed composition with no lanthanides in the lanthanide-poor component and a $\log_{10}(X_{\rm lan}) \sim -1.28$ lanthanide-rich component. Their mass estimates are smaller than those we derive for atomic data set ATOMIC, though this could be due to their radiative transfer simulations being run in 2D as opposed to 1D, which can lead to smaller mass estimates due to treatment of photon interaction between the two components (i.e., K. Kawaguchi et al. 2018). Additionally, the fixed higher $X_{\rm lan}$ in their lanthanide-rich component will cause more optical light to be reprocessed into IR for a longer time. To compensate, a faster lanthanide-rich component would cause a faster decline in IR bands to match AT2017gfo, possibly resulting in the finding of a higher velocity than our model-matching fits. As for the lanthanide-poor component, the lower characteristic velocity ($\Delta v \sim 0.07c$) would generate a longer-lasting optical transient and potentially "replenish" some of the additional optical light that had been reprocessed into IR due to the higher $X_{\rm lan}$ in the lanthanide-rich component.

Finally, we compare our results to that of the two-component fit from V. A. Villar et al. (2017). The total mass of the two-component model in V. A. Villar et al. (2017) is approximately double that of the model-matching estimates presented here, as well as a much faster lanthanide-rich component ($\Delta v \sim 0.1c$) and somewhat slower lanthanide-poor component ($\Delta v \sim 0.05c$). This may be a result of their wavelength-independent opacity models, which would underpredict the opacity at optical and UV wavelengths while overpredicting the opacity at IR wavelengths. As a result, less emission will be reprocessed into the IR, creating a brighter optical light curve and a fainter IR light curve. To create a sufficiently bright IR transient, the gray opacity scheme will require a more massive lanthanide-rich component. However, to prevent the model from remaining too bright for too long, the fitting procedure may have favored a higher velocity model.

5.2. "Error Estimation" Self-comparison

To more generally quantify how atomic data uncertainties affect KN parameter estimations, we consider each model in a given atomic data set and find a best-fitting model from the other two atomic data sets. We use the same grid used to "fit" the GW170817 data, and only use local thermalization efficiency prescription models. We again use a weighted χ^2 fitting (Equation (7)) to determine the best-fitting model with the weighting to equalize the importance of each band. Each model is fit using absolute magnitudes. Due to the large disagreement in optical data between atomic data sets HULLAC and ATOMIC with atomic data set Autostructure as well as avoid biasing due to similarities in the optical of atomic data sets HULLAC and ATOMIC from their shared nonlanthanide data, we only fit for J, H, and Ks bands. We apply this fitting method for models with $\log_{10}(X_{\rm lan}) \geqslant -4$, as the bound–bound transitions of lanthanides will eventually become subdominant to nonlanthanides at smaller values of $X_{\rm lan}$.

The baseline model has data sampled at a frequency of 1 day plus a δt determined randomly by a Gaussian distribution of $\mu = 0$ and $\sigma = 0.2$ to mimic a nightly observing campaign. Additionally, for each photometric point, we add Gaussian noise with standard deviation equal to the scatter of the approximately similar filters in GW170817.

Figure 12 shows the results of this exercise for each combination of mass and characteristic velocity with $\log_{10}(X_{\rm lan}) = -2$, -3, and -4 from the top row to bottom row. When using atomic data set HULLAC to fit models run with atomic data set ATOMIC and vice versa, there is good agreement in mass, velocity, and $X_{\rm lan}$ estimation overall for $\log_{10}(X_{\rm lan}) = -4$, -3. However, at higher characteristic velocities like 0.2 and $0.3c$, a ± 1 dex uncertainty in $X_{\rm lan}$ begins to emerge. Similarly, at low velocity-high mass end, a $\pm 0.01\,M_\odot$ (20%–25%) offset emerges.

Yet, the highest $X_{\rm lan}$ fitting reveals a much larger uncertainty with velocity estimations being incorrect by $\sim 0.1-0.2c$ and mass estimates off by $\pm 0.02\,M_\odot$ (25%–40%) for some of the highest mass models. For 8 out of the 20 models, atomic data set ATOMIC requires a smaller $X_{\rm lan}$ to reproduce a similar IR light curve to those made by atomic data set HULLAC, with most of those being at the higher velocity end. In the other direction, when fitting atomic data set ATOMIC models with those from atomic data set HULLAC always requires the highest $X_{\rm lan}$.

Atomic data set Autostructure consistently struggles to fit the light curves from atomic data sets HULLAC and ATOMIC, and vice versa. While the mass estimates are the most accurate, they still tend to be incorrect by $\sim 0.02\,M_\odot$ (25%–40%), and up to $0.05\,M_\odot$ (>100%). Figure 12 clearly shows a degeneracy between $X_{\rm lan}$ and velocity, with the lower $X_{\rm lan}$ models fitting lower velocities better because the IR peaks are more delayed in low $X_{\rm lan}$ models of atomic data set Autostructure, compared to the much more immediate brightening produced by atomic data sets HULLAC and ATOMIC. The faster atomic data set Autostructure models achieve their IR peaks much more rapidly, and so there are better fits at higher $X_{\rm lan}$. Despite the major discrepancy in $X_{\rm lan}$ of the base atomic data set Autostructure model and the ejecta parameters of the atomic data sets HULLAC and ATOMIC fits (7–8 dex), the reduced χ^2 is ~ 0.27, indicating a high quality fit. This discrepancy is reduced in the lower $X_{\rm lan}$ models, though at the cost of incorrectly

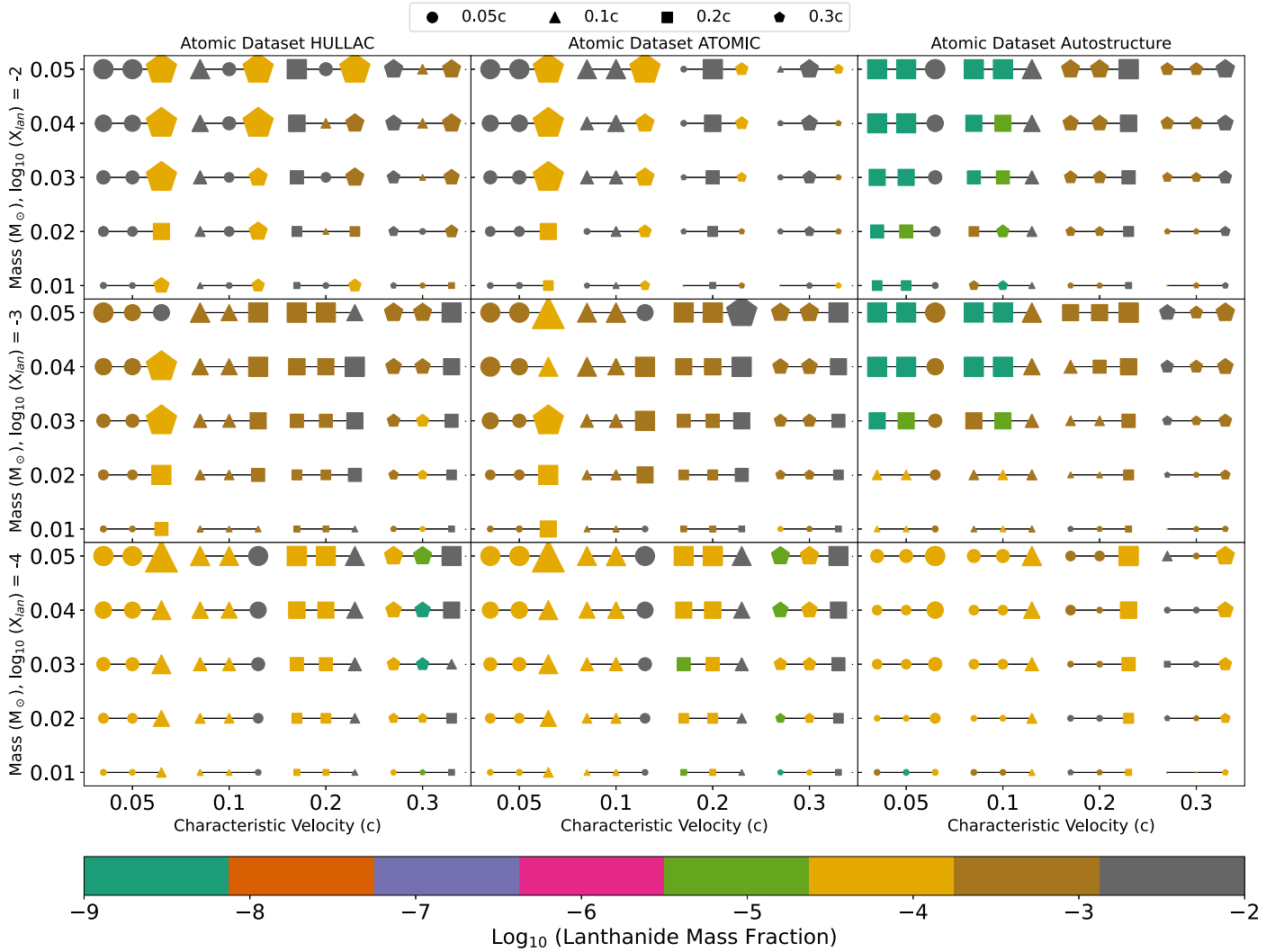

Figure 12. Best-fitting models for atomic data set HULLAC, ATOMIC, and Autostructure models for the left, middle, and right, respectively. At each point on the model grid, the left, middle, and right symbol connected by a line represent the best-fitting model from each atomic data set in the same order as the columns (thus the "correct" symbol is on the left, middle, and right for the left, middle, and right columns, respectively). Color corresponds to the best-fitting $X_{\rm lan}$, while a circle, triangle, square, and pentagon represent a best-fitting velocity of 0.05, 0.1, 0.2, and 0.3c, respectively. Size of the marker correlates to the best-fitting mass. Atomic data sets HULLAC and ATOMIC fit each other with the highest accuracy, though at higher velocities, a 1 dex discrepancy in $X_{\rm lan}$ emerges with atomic data set HULLAC underestimating $X_{\rm lan}$, and the highest $X_{\rm lan}$ models disagree on mass and velocity estimates by 25%–40% and 0.1–0.2c, respectively. Atomic data sets HULLAC and ATOMIC have very similar fits to atomic data set Autostructure models as they (i) require much lower $X_{\rm lan}$ and high velocities to match the IR of Autostructure models, (ii) tend to overestimate the velocity by 0.1–0.2c, and (iii) incorrectly estimate the mass by one grid step (20%–50%). When fitting other models with atomic data set Autostructure models, atomic data set Autostructure often overestimates the mass by as much as a factor of 3 at low velocities, and consistently struggles to fit the correct velocity at all.

estimating the velocity as almost all models are best fit by models of velocity 0.05c.

Velocity agreement improves at higher velocities and lower $X_{\rm lan}$, but $X_{\rm lan}$ estimates get worse at higher velocities. Mass estimates tend to consistently be off by ∼0.01 or 0.02 $M_\odot$ across all atomic data sets, though reaching as high as 0.07 $M_\odot$ for a 0.03 $M_\odot$ model. However, spectroscopy is capable of giving a direct measurement of the characteristic velocity and thus break uncertainties, making many of the error estimates for velocity moot. In cases where spectroscopy was not obtained or impossible to obtain, such as a target that is too faint or a KN that was discovered in the LSST archives, these errors may become applicable.

5.3. Impacts on Galactic Nucleosynthesis

Based on the systematic uncertainties in mass and $X_{\rm lan}$ estimates in the previous sections, here we propagate the impact of those uncertainties to conclusions about KN r-process as the source of galactic r-process elements. Following a prescription similar to that of S. Rosswog et al. (2017), we can approximate the amount of lanthanides in the Milky Way, assuming that all lanthanides come from a single type of event, as:

$$M_{\rm lan} = \mathcal{R} \times \overline{M_{\rm ej}} \times X_{\rm lan} \times \tau_{\rm MW}, \quad (8)$$

where $M_{\rm lan}$ is the total lanthanide mass in the Milky Way, $\mathcal{R}$ is the rate of mergers per year in the Milky Way, $\overline{M_{\rm ej}}$ is the average ejected mass, and $\tau_{\rm MW}$ is the age of the Milky Way.

Under this prescription, to achieve the same amount of lanthanides in the Milky Way, a decrease in the compact object merger rate would have to be compensated by a proportional increase in the typical mass of the ejecta and vice versa, assuming a constant $X_{\rm lan}$. J. Lippuner & L. F. Roberts (2015) calculate that, at most, material undergoing the r-process can

achieve $X_{\rm lan} \sim 35\%$, though the typical low Y_e material is much closer to 10%, placing an upper limit for that parameter.

Therefore, the errors presented above (Sections 4.3, 4.4, 5.1, 5.1.1, 5.2) directly translate into the same percent errors in the required compact object merger rate: a 0.75 dex uncertainty in $X_{\rm lan}$ translates to roughly a factor of 6 change in the compact object merger rate (assuming the same ejecta mass), and the 25%–40% mass error from atomic data as well as 30% error from thermalization efficiency would require a factor of $\sim$1.3 −1.4 change in compact merger rate.

To place these errors in context, currently the estimates of compact merger rates are 360–1800 events $\mathrm{Gpc^{-3}\,yr^{-1}}$ based on Chandra and XMM-Newton short gamma-ray bursts (A. Rouco Escorial et al. 2023), 10–1700 BNS merger events $\mathrm{Gpc^{-3}\,yr^{-1}}$ (90% confidence) based on LIGO rates (R. Abbott et al. 2023), and 244^{+325}_{-166} merger events $\mathrm{Gpc^{-3}\,yr^{-1}}$ based on population synthesis studies from C. Kim et al. (2015) and a conversion factor of 1.16×10^2 Milky Way-like galaxies $\mathrm{Mpc^{-3}}$ from J. Abadie et al. (2010), as discussed in S. Rosswog et al. (2017).

While there are still many other sources in error of the compact merger rate such as the opening angle distribution of gamma-ray burst jets or the minimum gamma-ray luminosity (A. Rouco Escorial et al. 2023), and assumptions about the underlying NS population-like mass and spin (R. Abbott et al. 2023), among those presented in this work the lanthanide mass fraction has the highest impact.

6. Conclusions

In this paper, we presented the systematic uncertainties in KN ejecta properties that arise from variance in thermalization-efficiency prescriptions and unknown lanthanide atomic data based on fitting light curves of both real KN data from AT2017gfo as well as cross-fitting synthetic light curve models. We presented KN models that span the expected ejecta mass, velocity, and $X_{\rm lan}$ range using three atomic data sets and two thermalization-efficiency prescriptions. We show that the typical errors quoted in parameter estimates (such as a 0.02, 0.05, 0.08 dex in mass error (M. Breschi et al. 2021; M. Ristić et al. 2023; P. T. H. Pang et al. 2023), 0.3 dex in $X_{\rm lan}$error (J. H. Gillanders et al. 2022), <3% in velocity error (M. Breschi et al. 2021) do not include the model uncertainties and are significantly smaller than the the 20%–50% uncertainty in mass caused by thermalization prescription and 25%–40% from atomic data uncertainty. $X_{\rm lan}$ can vary by 0.75 orders of magnitude for the lanthanide-rich component and as much as 5 orders of magnitude for the lanthanide-poor component by comparing model-matching fits of AT2017gfo light curves (the significantly higher uncertainty on the lanthanide-poor component is likely due to the subdominance of bound–bound transitions at such low $X_{\rm lan}$).

Fitting IR light curves with models generated from other atomic data sets reveals a typical mass error of 20%–40%, though the error can be as high as a factor of 3. Velocity errors are typically 0.1–0.2c ($\sim$100%), though spectroscopic follow-up would help to eliminate this uncertainty. Similarly, errors in $X_{\rm lan}$ are more severe at higher $X_{\rm lan}$, with a typical error of $\pm$1 order of magnitude.

The uncertainties derived in this work imply the total inferred lanthanide production of BNS mergers can vary by a factor of $\sim$6. Therefore, if BNS merger events are the sole contributor of lanthanides to the r-process enrichment of the Milky Way, the merger rate required to reproduce the abundances seen in the Milky Way have an additional uncertainty factor of $\sim$6.

While the work presented here identified a few sources of systematic uncertainties, there are still many other systematics that are worthwhile to explore further. NLTE effects, compositional gradients, asymmetries in the ejecta, variable radioactive heating rates, the inclusion of fission and fission fragments, and delayed thermalization may impact the light curves and spectral series substantially.

Spectral sequences will be able to reduce the impact of some, though not all, of the uncertainties presented in this work. Spectra can provide a much more direct estimate of ejecta velocities, inform viewing angle dependencies, and at late times, MIR spectra could constrain individual atomic abundances as well as inform atomic data modeling.

This work highlights the need for progress on both the theoretical and observational front to better constrain underlying KN physics. A nearby KN targeted by facilities such as JWST would provide ample data in the MIR to identify important lines and constrain atomic models, indicating the need for sufficient Target of Opportunity request availability. Further GRMHD simulations of compact object mergers containing a NS can constrain ejecta morphology and ejection mechanisms to inform radiative transfer models, and therefore make more realistic assumptions for more accurate models.

Acknowledgments

We thank the anonymous referee for suggestions which helped make the manuscript clearer. D.B. is partially supported by a NASA Future Investigators in NASA Earth and Space Science and Technology (FINESST) award No. 80NSSC23K1440. R.M. acknowledges support by the National Science Foundation under award No. AST-2221789 and AST-2224255. The TReX team at UC Berkeley is partially funded by the Heising–Simons Foundation under grant 2021-3248 (PI: Margutti). D.K. is supported in part by the U.S. Department of Energy, Office of Science, Division of Nuclear Physics, under award numbers DE-SC0004658 and DE-SC0024388, and by the Simons Foundation (award number 622817DK). This research used the Savio computational cluster resource provided by the Berkeley Research Computing program at the University of California, Berkeley (supported by the UC Berkeley Chancellor, Vice Chancellor for Research, and Chief Information Officer).

Software: numpy (C. R. Harris et al. 2020), `sedona` (D. Kasen et al. 2006; N. Roth & D. Kasen 2015), astropy (Astropy Collaboration et al. 2013, 2018, 2022), matplotlib (J. D. Hunter 2007), h5py.

Data Availability

All spectra are deposited to Zenodo doi:10.5281/zenodo.13743449.

ORCID iDs

D. Brethauer https://orcid.org/0000-0001-6415-0903
D. Kasen https://orcid.org/0000-0002-5981-1022
R. Margutti https://orcid.org/0000-0003-4768-7586
R. Chornock https://orcid.org/0000-0002-7706-5668

References

Abadie, J., Abbott, B. P., Abbott, R., et al. 2010, CQGra, 27, 173001
Abbott, B. P., Abbott, R., Abbott, T. D., et al. 2017, PhRvL, 119, 161101
Abbott, R., Abbott, T. D., Acernese, F., et al. 2023, PhRvX, 13, 011048
Alexander, K. D., Berger, E., Fong, W., et al. 2017, ApJL, 848, L21

Andreoni, I., Ackley, K., Cooke, J., et al. 2017, PASA, 34, e069
Andreoni, I., Coughlin, M. W., Almualla, M., et al. 2022a, ApJS, 258, 5
Andreoni, I., Margutti, R., Salafia, O. S., et al. 2022b, ApJS, 260, 18
Arcavi, I., Hosseinzadeh, G., Howell, D. A., et al. 2017, Natur, 551, 64
Asplund, M., Grevesse, N., Sauval, A. J., & Scott, P. 2009, ARA&A, 47, 481
Astropy Collaboration, Price-Whelan, A. M., Lim, P. L., et al. 2022, ApJ, 935, 167
Astropy Collaboration, Price-Whelan, A. M., Sipőcz, B. M., et al. 2018, AJ, 156, 123
Astropy Collaboration, Robitaille, T. P., Tollerud, E. J., et al. 2013, A&A, 558, A33
Badnell, N. R. 2011, CoPhC, 182, 1528
Barnes, J., Kasen, D., Wu, M.-R., & Martínez-Pinedo, G. 2016, ApJ, 829, 110
Bar-Shalom, A., Klapisch, M., & Oreg, J. 2001, JQSRT, 71, 169
Breschi, M., Perego, A., Bernuzzi, S., et al. 2021, MNRAS, 505, 1661
Bulla, M. 2023, MNRAS, 520, 2558
Chornock, R., Berger, E., Kasen, D., et al. 2017, ApJL, 848, L19
Coughlin, M. W., Dietrich, T., Doctor, Z., et al. 2018, MNRAS, 480, 3871
Coulter, D. A., Foley, R. J., Kilpatrick, C. D., et al. 2017, Sci, 358, 1556
Cowperthwaite, P. S., Berger, E., Villar, V. A., et al. 2017, ApJL, 848, L17
Cowperthwaite, P. S., Villar, V. A., Scolnic, D. M., & Berger, E. 2019, ApJ, 874, 88
Díaz, M. C., Macri, L. M., Garcia Lambas, D., et al. 2017, ApJL, 848, L29
Drout, M. R., Piro, A. L., Shappee, B. J., et al. 2017, Sci, 358, 1570
Eichler, D., Livio, M., Piran, T., & Schramm, D. N. 1989, Natur, 340, 126
Evans, P. A., Cenko, S. B., Kennea, J. A., et al. 2017, Sci, 358, 1565
Fontes, C. J., Fryer, C. L., Hungerford, A. L., Wollaeger, R. T., & Korobkin, O. 2020, MNRAS, 493, 4143
Freiburghaus, C., Rosswog, S., & Thielemann, F. K. 1999, ApJL, 525, L121
Fryer, C. L., Hungerford, A. L., Wollaeger, R. T., et al. 2024, ApJ, 961, 9
Gillanders, J. H., Smartt, S. J., Sim, S. A., Bauswein, A., & Goriely, S. 2022, MNRAS, 515, 631
Goldstein, A., Veres, P., Burns, E., et al. 2017, ApJL, 848, L14
Hallinan, G., Corsi, A., Mooley, K. P., et al. 2017, Sci, 358, 1579
Harris, C. R., Millman, K. J., van der Walt, S. J., et al. 2020, Natur, 585, 357
Hillier, D. J., & Lanz, T. 2001, in ASP Conf. Ser. 247, Spectroscopic Challenges of Photoionized Plasmas, ed. G. Ferland & D. W. Savin (San Francisco, CA: ASP), 343
Holmbeck, E. M., Barnes, J., Lund, K. A., et al. 2023, ApJL, 951, L13
Hotokezaka, K., & Nakar, E. 2020, ApJ, 891, 152
Hotokezaka, K., Piran, T., & Paul, M. 2015, NatPh, 11, 1042
Hotokezaka, K., Tanaka, M., Kato, D., & Gaigalas, G. 2022, MNRAS, 515, L89
Hotokezaka, K., Tanaka, M., Kato, D., & Gaigalas, G. 2023, MNRAS, 526, L155
Hu, L., Wu, X., Andreoni, I., et al. 2017, SciBu, 62, 1433
Hunter, J. D. 2007, CSE, 9, 90
Ji, A. P., Frebel, A., Chiti, A., & Simon, J. D. 2016, Natur, 531, 610
Kasen, D., Badnell, N. R., & Barnes, J. 2013, ApJ, 774, 25
Kasen, D., Metzger, B., Barnes, J., Quataert, E., & Ramirez-Ruiz, E. 2017, Natur, 551, 80
Kasen, D., Thomas, R. C., & Nugent, P. 2006, ApJ, 651, 366
Kasliwal, M. M., Kasen, D., Lau, R. M., et al. 2022, MNRAS, 510, L7
Kasliwal, M. M., Nakar, E., Singer, L. P., et al. 2017, Sci, 358, 1559
Kawaguchi, K., Shibata, M., & Tanaka, M. 2018, ApJL, 865, L21
Kim, C., Perera, B. B. P., & McLaughlin, M. A. 2015, MNRAS, 448, 928
Lattimer, J. M., & Schramm, D. N. 1974, ApJL, 192, L145
Lattimer, J. M., & Schramm, D. N. 1976, ApJ, 210, 549
Levan, A. J., Gompertz, B. P., Salafia, O. S., et al. 2024, Natur, 626, 737
Lippuner, J., & Roberts, L. F. 2015, ApJ, 815, 82
Lipunov, V. M., Gorbovskoy, E., Kornilov, V. G., et al. 2017, ApJL, 850, L1
Margutti, R., Berger, E., Fong, W., et al. 2017, ApJL, 848, L20
Margutti, R., & Chornock, R. 2021, ARA&A, 59, 155
Margutti, R., Cowperthwaite, P., Doctor, Z., et al. 2018, arXiv:1812.04051
Nakar, E. 2020, PhR, 886, 1
Narayan, R., Paczynski, B., & Piran, T. 1992, ApJL, 395, L83
Pang, P. T. H., Dietrich, T., Coughlin, M. W., et al. 2023, NatCo, 14, 8352
Pian, E., D'Avanzo, P., Benetti, S., et al. 2017, Natur, 551, 67
Pozanenko, A. S., Barkov, M. V., Minaev, P. Y., et al. 2018, ApJL, 852, L30
Qian, Y. Z., & Wasserburg, G. J. 2007, PhR, 442, 237
Radice, D., & Bernuzzi, S. 2023, ApJ, 959, 46
Radice, D., Bernuzzi, S., & Perego, A. 2020, ARNPS, 70, 95
Ralchenko, Y., Olsen, K., Fontes, C., et al. 2021, NIST-LANL Lanthanide/Actinide Opacity Database, National Institute of Standards and Technology, doi:10.18434/mds2-2375
Ristić, M., O'Shaughnessy, R., Villar, V. A., et al. 2023, PhRvR, 5, 043106
Rosswog, S., Feindt, U., Korobkin, O., et al. 2017, CQGra, 34, 104001
Rosswog, S., Liebendörfer, M., Thielemann, F. K., et al. 1999, A&A, 341, 499
Rosswog, S., Sollerman, J., Feindt, U., et al. 2018, A&A, 615, A132
Roth, N., & Kasen, D. 2015, ApJS, 217, 9
Rouco Escorial, A., Fong, W., Berger, E., et al. 2023, ApJ, 959, 13
Sarin, N., & Rosswog, S. 2024, ApJL, 973, L24
Savchenko, V., Ferrigno, C., Kuulkers, E., et al. 2017, ApJL, 848, L15
Shappee, B. J., Simon, J. D., Drout, M. R., et al. 2017, Sci, 358, 1574
Shingles, L. J., Collins, C. E., Vijayan, V., et al. 2023, ApJL, 954, L41
Simmerer, J., Sneden, C., Cowan, J. J., et al. 2004, ApJ, 617, 1091
Smartt, S. J., Chen, T. W., Jerkstrand, A., et al. 2017, Natur, 551, 75
Sneppen, A., & Watson, D. 2023, A&A, 675, A194
Soares-Santos, M., Holz, D. E., Annis, J., et al. 2017, ApJL, 848, L16
Sobolev, V. V. 1960, SvA, 4, 372
Sugita, S., Kawai, N., Nakahira, S., et al. 2018, PASJ, 70, 81
Symbalisty, E., & Schramm, D. N. 1982, ApL, 22, 143
Tanaka, M., Kato, D., Gaigalas, G., & Kawaguchi, K. 2020, MNRAS, 496, 1369
Tanaka, M., Kato, D., Gaigalas, G., et al. 2018, ApJ, 852, 109
Tanvir, N. R., Levan, A. J., González-Fernández, C., et al. 2017, ApJL, 848, L27
Tarumi, Y., Hotokezaka, K., Domoto, N., & Tanaka, M. 2023, arXiv:2302.13061
Troja, E., Piro, L., van Eerten, H., et al. 2017, Natur, 551, 71
Utsumi, Y., Tanaka, M., Tominaga, N., et al. 2017, PASJ, 69, 101
Valenti, S., Sand, D. J., Yang, S., et al. 2017, ApJL, 848, L24
Villar, V. A., Guillochon, J., Berger, E., et al. 2017, ApJL, 851, L21
Wallner, A., Faestermann, T., Feige, J., et al. 2015, NatCo, 6, 5956
Watson, D., Hansen, C. J., Selsing, J., et al. 2019, Natur, 574, 497
Wollaeger, R. T., Fryer, C. L., Chase, E. A., et al. 2021, ApJ, 918, 10
Wollaeger, R. T., Korobkin, O., Fontes, C. J., et al. 2018, MNRAS, 478, 3298
Zhu, Y. L., Lund, K. A., Barnes, J., et al. 2021, ApJ, 906, 94